

EvalMVX: A Unified Benchmarking for Neural 3D Reconstruction under Diverse Multiview Setups

Zaiyan Yang¹ Jieji Ren² Xiangyi Wang¹ Zonglin Li¹
Xu Cao³ Heng Guo^{1,4*} Zhanyu Ma¹ Boxin Shi⁵

¹Beijing University of Posts and Telecommunications, Beijing, China

²School of Mechanical Engineering, Shanghai Jiao Tong University, Shanghai, China

³Independent Researcher

⁴Xiong'an Aerospace Information Research Institute, Xiong'an, China

⁵State Key Laboratory of Multimedia Information Processing, School of Computer Science
Peking University, Beijing, China

Abstract

Recent advancements in neural surface reconstruction have significantly enhanced 3D reconstruction. However, current real world datasets mainly focus on benchmarking multiview stereo (MVS) based on RGB inputs. Multiview photometric stereo (MVPS) and multiview shape from polarization (MVSfP), though indispensable on high-fidelity surface reconstruction and sparse inputs, have not been quantitatively assessed together with MVS. To determine the working range of different MVX (MVS, MVSfP, and MVPS) techniques, we propose EvalMVX, a real-world dataset containing 25 objects, each captured with a polarized camera under 20 varying views and 17 light conditions including OLAT and natural illumination, leading to 8,500 images. Each object includes aligned ground-truth 3D mesh, facilitating quantitative benchmarking of MVX methods simultaneously. Based on our EvalMVX, we evaluate 13 MVX methods published in recent years, record the best-performing methods, and identify open problems under diverse geometric details and reflectance types. We hope EvalMVX and the benchmarking results can inspire future research on multiview 3D reconstruction.

1. Introduction

3D reconstruction from multiview images is a foundational problem in computer vision, critical for applications such as virtual reality, appearance editing, and more. The most common setup of multiview 3D reconstruction is multiview stereo (MVS) [28, 39, 40], which takes multiview RGB images as input for recovering surface shape. Consider-

ing the complex reflectance, multiview shape from polarization (MVSfP) [10, 14, 23] taking multiview polarization images as input is proposed, which is shown to be effective in reflective surface recovery even under sparse capture due to additional photometric and geometric cues from polarization images. Besides, multiview photometric stereo (MVPS) [3, 4, 19] excels in detailed surface reconstruction for general reflectance, leveraging surface normal maps estimated from images under varying illumination.

With the rapid development of MVX (*i.e.*, MVS, MVPS, and MVSfP) techniques since the proposition of NeRF [31], understanding the working range and trade-offs of each approach is essential. For instance, while both PET-NeuS [41] and SuperNormal [4] claim high-fidelity surface reconstruction, they differ in setup—MVS and MVPS, respectively. Identifying the balance between capture effort and reconstruction quality across setups is crucial for guiding users in selecting the optimal method and configuration for 3D surface reconstruction tasks. Achieving this goal necessitates a dedicated design of a real-world datasets which can jointly evaluating different setups in a quantitative manner.

However, existing real-world datasets primarily benchmark only one of the MVX techniques. For example, datasets such as DTU [18], MVImageNet [46], and Mobilebrick [24] focus on evaluating MVS; DiLiGenT-MV [25], OpenIllumination [27], and ReLight My NeRF [35] contain multiview and multilight images for MVPS evaluation; NeRSP [14] and PANDORA [10] capture multiview polarization images for assessing MVSfP. To the best of our knowledge, there is no dataset capable of benchmarking MVS, MVSfP, and MVPS simultaneously for identifying their application scenarios. Additionally, existing

datasets [27, 35, 36, 46] lack aligned ground-truth (GT) shapes essential for quantitative surface reconstruction evaluation. One solution is using synthetic datasets such as NeRF-synthetic [31]. However, synthetic datasets struggle to replicate complex physical characteristics and noise patterns, resulting in a domain gap between synthetic evaluations and real-world performance.

To address these problems, we present EvalMVX, the first real-world dataset with aligned GT shapes designed for quantitatively benchmarking MVS, MVSP, and MVPS simultaneously. As shown in Fig. 1, EvalMVX captures 25 objects with diverse shapes and reflectances. From left to right, more details occur on surface shape, while the reflectance changes from simple diffuse to complex specular and metallic from top to bottom. For each object, we capture 20 views using a polarization camera. Each with one image taken under environment-light and 16 images taken in a one-light-at-a-time (OLAT) manner. We scan a 3D mesh and propose an inverse silhouette rendering pipeline to align the 3D scan with the camera views. Given multiview polarized images captured under environment light and the corresponding GT shape, we evaluate the performance of MVSP. Additionally, using unpolarized images decomposed from the polarization data, we benchmark MVS under static environment light and MVPS under varying illuminations. In this way, all MVX methods can be quantitatively evaluated alongside EvalMVX on the same objects observed from identical viewpoints.

Based on EvalMVX, we benchmark 4 MVS methods, 4 MVPS methods, and 3 MVSP methods and quantitatively evaluate each in terms of shape reconstruction accuracy and computational efficiency. For each object, we also report the best-performing method to highlight the trade-offs between shape and reflectance complexity, reconstruction accuracy, and capture effort.

Contributions This paper introduces EvalMVX, the first real-world dataset designed to evaluate MVS, MVSP, and MVPS methods simultaneously by capturing multiview polarization images under controlled illumination. With aligned GT shapes, our benchmark provides a quantitative assessment of MVX methods, establishing their working ranges for various shapes and reflectances.

2. Related works

We briefly summarize recent advancements in multiview stereo (MVS), multiview photometric stereo (MVPS), and multiview shape from polarization (MVSP), highlighting their input settings and focuses. Additionally, we review real-world datasets collected for evaluating MVX methods.

2.1. MVX methods

Multiview Stereo recovers 3D shapes from RGB images captured at different camera poses. Traditional methods like COLMAP [34] rely on Structure from Motion, requiring feature correspondences across views. Recent methods, such as NeuS [39] and VolSDF [45], improve MVS by leveraging differentiable volume rendering and neural implicit surface representations. For reflective surfaces, Ref-NeuS [13] and NeRO [28] use integrated positional encoding [37] to disentangle shape, reflectance, and illumination. To handle sparse views, SparseNeuS [30] and S-VolSDF [42] incorporate generalizable priors from image features and probability volume to gain the robustness of estimated shape. PET-NeuS [41] and Neuralangelo [26] apply positional encoding tri-planes and a coarse-to-fine optimization strategy on hash grids, shown to be effective in recovering geometric details. For efficiency, NeuS2 [40] integrates multi-resolution hash encoding and a CUDA implementation to accelerate NeuS [39]. Meanwhile, R-3DGS [12] and GaussianSurfels [9] accelerate reconstruction by incorporating 3D Gaussian Splatting (3DGS) [20].

Multiview photometric stereo recovers surface shape from images captured under varying light and viewpoints, offering advantages for detailed shape recovery. PS-NeRF [44] estimates surface normals from multi-light images using photometric stereo, then uses them to regularize the neural radiance field. UA-MVPS [19] address unreliable surface estimates problem by introducing uncertainty. SuperNormal [4] and RnbNeuS [3] first estimate per-view surface normals with off-the-shelf photometric stereo method [17] and refine 3D surface shape through multiview surface normal consistency. Instead of per-view multi-light capture, VMINer [11] and WildLight [8] capture flash and no-flash image pairs at varying viewpoints, improving shape reconstruction accuracy while maintaining a practical setup. Unlike above methods that require per-scene optimization, MVPSNet [47] trains a generalizable MVPS network capable of efficient depth and normal prediction.

Multiview shape from polarization offers advantages over MVS as angle of polarization (AoP) provides geometric cue of surface normals. Based on this property, PANDORA [10] achieves shape recovery and radiance decomposition by minimizing the difference between rendered and observed Stokes vectors. MVAS [6] leverages azimuth angle consistency across views to recover surface shape from AoP. NeRSP [14] combines the photometric cue and geometric cue from polarization images and achieves reflective surface reconstruction under sparse polarization. PISR [7] boosts the efficiency of MVSP by introducing hash-grid-based neural SDF. NeISF [23] proposes a neural implicit Stokes field and shows the merit of MVSP in handling

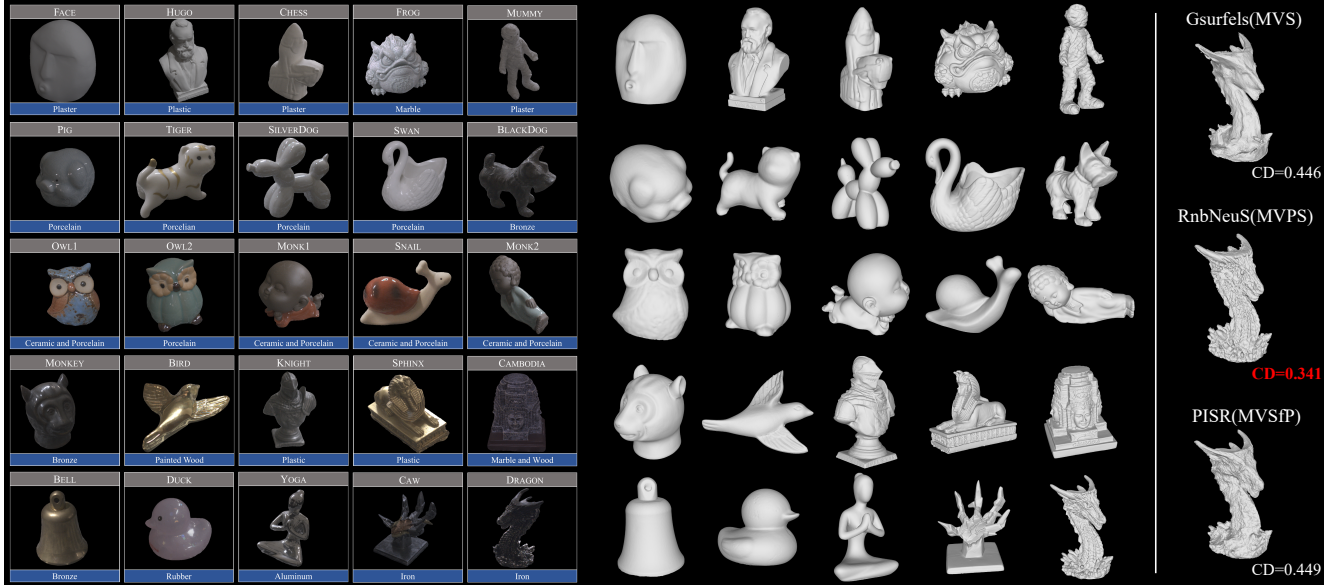


Figure 1. Dataset overview. EvalMVX contains 25 objects (left), covering diverse shapes and materials. From top to bottom, the materials range from simple diffuse to complex metallic and reflective ones, while the complexity of object shapes increases from left to right. With aligned GT shapes (middle), we can quantitatively evaluate MVX methods on the same object (right) and reveal their performance on detailed shape recovery and robustness against complex material.

scenes containing strong inter-reflections.

2.2. MVX datasets

As shown in Table 1, we summarize public real-world datasets for evaluating MVX in recent years. Below, we briefly describe each dataset, categorized by its target benchmark tasks.

Multiview stereo. DTU [18] is commonly used to benchmark MVS methods under environment illuminations. Stanford-ORB [22] scans 14 objects and aligns scanned meshes with captured multiview images for quantitative evaluation. Mobilebrick [24] captures images of 153 LEGO models where 3D GT shapes can be obtained without using a scanner. Objects with Lighting [36] collects images captured under varying poses and illuminations to evaluate the performance of MVS at different natural scenes. To expand the scale of MVS dataset, MVImageNet [46] captures 220K objects from 238 classes, leading to 6.5 million frames from 219, 188 videos. CO3D [33] collects 1.5 million frames from 19, 000 videos across 50 object categories with accurate camera poses and the GT 3D point clouds. OmniObject3D[43] provides a large vocabulary of 6, 000 high-quality real-scanned 3D objects across 190 categories.

Multiview photometric stereo. DiLiGenT-MV [25] is the first real-world dataset dedicated to benchmarking MVPS, comprising 5 objects captured from 20 views, with each view illuminated by 96 OLAT sources in a darkroom.

ReLight My NeRF [35] and OpenIllumination [27] expand the scale of DiLiGenT-MV [25] to 20 and 64 objects, respectively. However, the GT shapes are not provided for quantitative evaluation. Skoltech3D[38] offers 1.4 million images of 107 scenes captured under 100 views and 14 lighting conditions using 7 different sensors (*e.g.*, Kinect, structured-light scanner), covering diverse shapes and materials. The above datasets can evaluate MVPS based on general unknown illumination settings [17].

Multiview shape from polarization. Different from MVS and MVPS, benchmarking MVSfP requires specific polarization camera, making the scale of existing real-world MVSfP dataset small. PANDORA [10] captures 3 objects, each captured with 35 views under natural illumination with a snapshot polarization camera. However, the GT shapes are not provided. To handle this problem, NeRSP [14] and PISR [7] capture 4 objects each, aligning GT shapes with the captured images. By using a polarization image formation model, unpolarized images can be extracted from the captured polarization ones, allowing these datasets to support both MVSfP and MVS benchmarking.

Despite substantial efforts in real-world dataset collection, quantitatively evaluating MVS, MVPS, and MVSfP simultaneously remains an open problem. This requires aligned GT 3D shapes, varied illuminations from both environment light and OLAT, and a polarization camera. Our EvalMVX is shown to be the first dataset to address these needs by capturing 25 objects with a snapshot polarization

Table 1. Summary of MVX datasets and their contents.

Dataset	EvalMVS	EvalMVPS	EvalMVSfP	3D GT	#Objects	#Lights	#Views
DTU [18]	✓	×	×	Point cloud	80	1/7 Env. ^a	49~64
Mobilebrick [24]	✓	×	×	Mesh	153	1 Env.	30~134
Stanford-ORB [22]	✓	×	×	Mesh	14	3/7 Env.	70
Objects with Lighting [36]	✓	×	×	None	8	3/72 Env.	42~67
CO3D [33]	✓	×	×	Point cloud	19K	Env. (Case dependent)	Case dependent
MVImageNet [46]	✓	×	×	None	220K	Env. (Case dependent)	Case dependent
OmniObject3D[43]	✓	×	×	Mesh	6k	Env. (Case dependent)	100
DiLiGenT-MV [25]	×	✓	×	Mesh	5	96 OLAT ^b	20
OpenIllumination [27]	×	✓	×	None	64	13 PAT ^c + 142 OLAT	72
ReLight My NeRF [35]	×	✓	×	None	20	40 OLAT	50
Skoltech3D[38]	✓	✓	×	Mesh	107	14 Env.	100
PANDORA Dataset [10]	✓	×	✓	None	3	1 Env.	35
NeRSP Dataset [14]	✓	×	✓	Mesh	5	1 Env.	6
PISR Dataset [7]	✓	×	✓	Mesh	4	1 Env.	40
EvalMVX	✓	✓	✓	Mesh	25	16 OLAT + 1 Env.	20

[a] Env: Environment light; [b] OLAT: One light at a time; [c] PAT: Pattern illumination.

camera under 16 OLATs and one static environment light.

3. EvalMVX

This paper aims to benchmark MVX methods comprehensively across various configurations. From a sensor perspective, a polarization camera is essential for evaluating both MVSfP and MVS methods. From an illumination standpoint, images captured from the same view under varying OLAT and static environment light are necessary to assess both MVS and MVPS methods. Finally, for shape and reflectance, selecting objects that range from simple, smooth shapes with diffuse reflectance to complex, detailed shapes with specular reflectance allows us to effectively determine the working ranges of different MVX methods.

3.1. Data capture

Capture Setup. As shown in Fig. 2, the object is placed on a marker board for intrinsic and extrinsic camera calibration. A 3D-printed rig holds 16 high-power LEDs arranged to maintain fixed relative positions between the LEDs and the camera. We use a Lucid Triton RGB polarization camera¹ equipped with a 16mm lens to capture snapshot polarization images under different viewpoints and illumination conditions. For each view, we first capture a polarization image at a resolution of 2448×2048 under environment light. Then, we sequentially capture images with each LED toggled on and off. By subtracting the environment-light image, we obtain OLAT images for MVPS. After the multi-illumination capture at one viewpoint, we move the light-camera rig around the object and repeat the process. The object remains static throughout this multiview, multi-light

acquisition. *Further details about camera poses and LEDs positions are provided in supplementary material.*

Object selection. As shown in Fig. 1, we choose 25 objects with diverse reflectances, containing **diffuse** surfaces such as FACE and MUMMY; **specular** surfaces such as PIG and MONKEY; **metallic** surfaces such as BELL; and a **translucent** surface DUCK. The objects are roughly ordered from top to bottom by increasing reflectance complexity. The object shapes in EvalMVX span a range from smooth surfaces, such as FACE and PIG, to highly detailed, complex geometries like CAMBODIA and DRAGON.

3.2. Data processing

Polarized image processing. We use a snapshot polarization camera to capture 16-bit raw image. Due to the structure of the Bayer filter, the raw image records image observations under different polarized directions of light, specifically at angles of 0° , 45° , 90° , and 135° , leading to four directional polarized images after demosaicing. As shown in Fig. 2, based on these four images, we calculate stokes vectors (s_0, s_1, s_2, s_3) , which are defined as

$$\begin{cases} s_0 = \frac{1}{2} (I_0 + I_{45} + I_{90} + I_{135}), \\ s_1 = I_0 - I_{90}, \\ s_2 = I_{45} - I_{135}, \end{cases} \quad (1)$$

where s_0 represents the total intensity of the light. The elements s_1 and s_2 describe the linear polarization components in the horizontal-vertical and $+45^\circ / -45^\circ$ directions, respectively. We neglect circularly polarized light and set $s_3 = 0$. Given Stokes vectors, we compute AoP ϕ and degree of polarization (DoP) as follows:

$$\phi = \frac{1}{2} \arctan \left(\frac{s_2}{s_1} \right), \quad \rho = \frac{\sqrt{s_1^2 + s_2^2}}{s_0}. \quad (2)$$

¹<https://thinklucid.com/product/triton-5-mp-polarization-camera/>

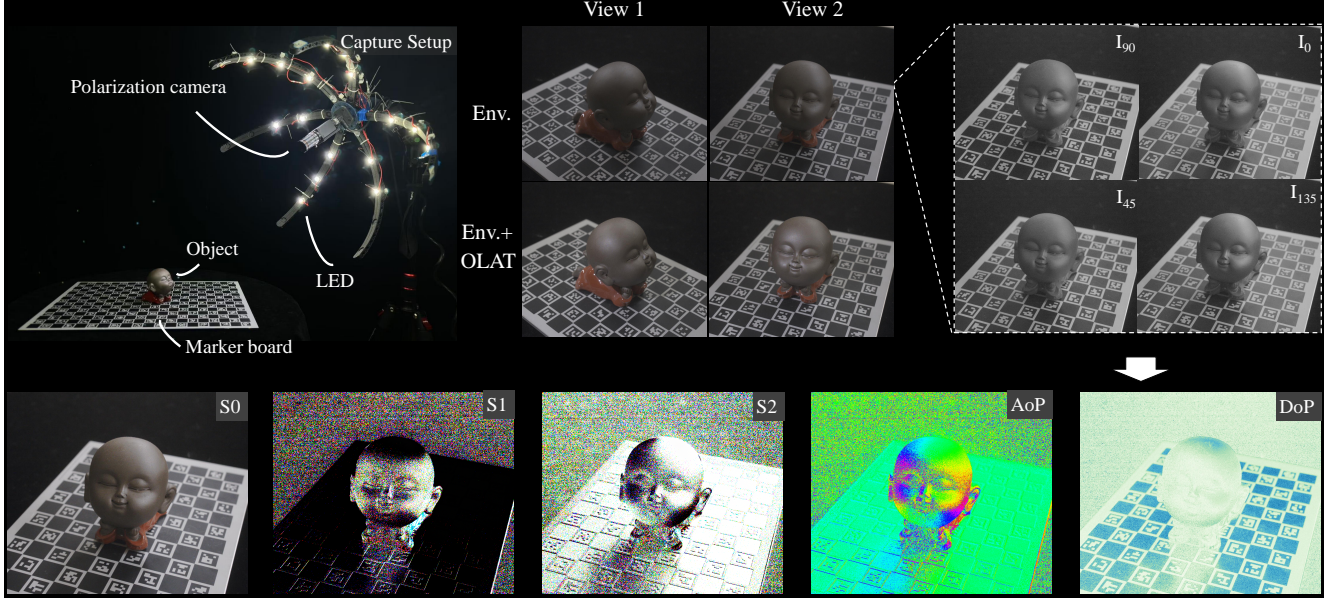


Figure 2. Capture setup and data processing of EvalMVX. **(Top)** Our capture system contains a polarization camera and 16 evenly distributed LEDs for recording multiview and multi-light images. **(Bottom)** Polarization information can be extracted from the snapshot polarization image.

The polarization images, stokes vectors, and the AoP and DoP maps are used as input for MVSfP.

Mask segmentation and camera poses calibration. Since existing MVX methods such as SuperNormal [4] require multiview object masks as input, we employed Segment Anything Model (SAM) [21] to perform silhouette mask segmentation. We use Metashape² to jointly estimate the camera’s intrinsic and extrinsic parameters, specifying the physical size of an Aruco Marker calibration board to recover the actual scale of the reconstructed shape.

3.3. GT shape alignment

We first scan the surface shape using a shining 3D EinScan-SP scanner³. Then we perform a coarse alignment between the scanned mesh and the dense reconstruction generated by Metashape using ICP algorithm [1]. To further align camera poses $[\hat{\mathbf{R}}_i, \hat{\mathbf{t}}_i]$ with the scanned mesh, we employ a differentiable render Pytorch3D [32] to minimize the difference between the rendered and observed object mask, *i.e.*

$$\min_{\{\hat{\mathbf{R}}_i, \hat{\mathbf{t}}_i\}_{i=1}^K} \sum_{i=1}^K \text{BCE} \left(f_M(\mathbf{X}; \hat{\mathbf{R}}_i, \hat{\mathbf{t}}_i), \mathbf{M}_i \right), \quad (3)$$

where $\text{BCE}(\cdot)$ denotes the binary cross entropy loss to measure the difference between rendered masks by project-

²Agisoft (2024) Agisoft Metashape. <https://www.agisoft.com/>

³EinScan SP Scanner <https://www.einscan.com/einscan-sp/>

ing mesh \mathbf{X} at different camera poses and the corresponding observed mask \mathbf{M}_i . Given aligned mesh and poses, we use Blender [2] to render surface normal maps as the “GT”. *More detail of our GT alignment process and the quantitative evaluation of the alignment quality can be found in our supplementary material.*

4. Benchmark evaluations

This section showcases the benchmark results for MVX methods using EvalMVX.

4.1. Baseline methods & evaluation metric

We select NeuS2 [40], an enhanced version of classical MVS method NeuS [39], along with its extensions for detailed surface recovery (PET-NeuS [41]) and reflective surface recovery (NeRO [28]). In addition, we include GaussianSurfels [9] adopting 3D Gaussian Splatting (3DGS) [20] to speed up MVS. For MVPS, we choose the state-of-the-art (SOTA) methods SuperNormal [4] and RnbNeuS [3], utilizing Uni-MS-PS [15] to estimate per-view surface normals from images captured under varying light conditions. We also include WildLight [8] and VMIner [11], where the flash image input is assigned as the one illuminated by the LED closest to the camera. For MVSfP, we select the SOTA methods MVAS [6], NeRSP [14], and PISR [7]. *Complete qualitative evaluations mesh visualizations, evaluation results on additional baselines including NeuS [39] and NeDUF [29], are provided in the supplementary material.*

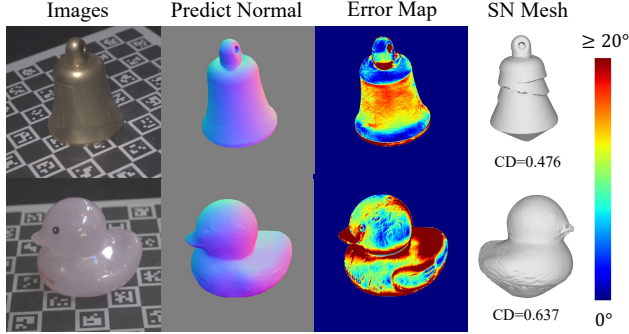


Figure 3. Inaccurate surface normal inputs from Uni-MS-PS [15] due to complex reflectance influence the shape recovery from SuperNormal [4].

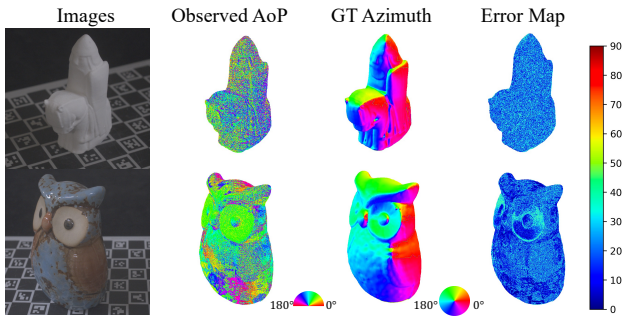


Figure 4. The difference between the real-captured AoP map and azimuth map due to sensor noise degrades the performance of MVSfP methods.

4.2. Overview of benchmark results

In this section, we discuss shape reconstruction results for methods at each MVX setup, followed by a working range analysis across different MVX setups.

MVPS methods. As shown in Table 2, SuperNormal [4] achieves the lowest or second-lowest CD on most objects, ranking as the SOTA in both median and average CD. Leveraging images captured under varying illumination, photometric stereo proves effective in handling diverse reflectance properties, and surface normals offer rich geometric cues for accurate and robust reconstruction. SuperNormal [4] integrates surface normal inputs and multi-resolution hash encoding, enabling high-fidelity surface recovery and demonstrating strong robustness to both diffuse (*e.g.* FROG) and specular (*e.g.* SPHINX) materials.

Despite the success of SuperNormal [4], we observe failure cases on metallic objects (*e.g.* BELL) and translucent objects (*e.g.* DUCK). As shown in Fig. 3, the input surface normals estimated by the learning-based photometric stereo method Uni-MS-PS [15] are less accurate due to complex reflectance. This limitation also propagates to RnbNeuS [3], which relies on Uni-MS-PS [15] for surface normal input.

On the other hand, WildLight [8] achieves the smallest average CD and second-smallest median CD among all methods, showing competitive results using only flash/no-flash image pairs. Unlike SuperNormal [4], which requires multiple illuminations, WildLight [8] demonstrates that a minimal two-shot setup with controlled light can reduce shape-reflectance ambiguity, providing high-quality reconstruction in a practical setting. In addition, since WildLight [8] is a self-supervised method based on inverse rendering, the shape estimation of BELL and DUCK is free from the error brought by the learning-based photometric stereo [15].

MVS Methods. As shown in Table 2, NeRO [28] achieves the lowest or second-lowest CD on 9 out of 25 objects, particularly excelling on highly reflective metallic surfaces such as SILVERDOG and YOGA. Its use of split-sum approximation and integrated directional encoding (IDE) enables more accurate modeling of specular reflections. However, NeRO [28] performs less effectively on diffuse surfaces like FACE and CHESS, likely due to its sensitivity to static environmental illumination, as noted in the original paper.

PET-NeuS [41] enhances NeuS [39] for high-fidelity surface reconstruction through positional encoding tri-planes. However, we observe that PET-NeuS [41] can produce overly rough meshes (*e.g.* DUCK) (see supplementary material), as its highly expressive network structure may overfit and hallucinate details. Additionally, the positional encoding tri-planes module seems to make it less robust on reflective surfaces, as observed in BIRD and BELL. GaussianSurfels [9] prioritizes fast reconstruction but produces less accurate results compared to NeuS2 [40] and NeRO [28]. A key limitation is its surfel-based representation, which lacks a unified modeling of volume density, depth, and surface normals offered by SDF-based approaches.

MVSfP Methods. Among MVSfP methods, PISR [7] stands out as the SOTA. Leveraging polarization images, MVSfP methods exhibit robust performance on surfaces with complex reflectance properties, such as the MONKEY and DUCK. In contrast to RGB-based methods, which often struggle with multiview consistency on non-Lambertian surfaces, AoP maps used in MVSfP inherently constrain the azimuth component of surface normals, thereby enhancing the robustness and accuracy of surface reconstruction under challenging reflectances.

However, as shown in Fig. 4, the relationship between the observed AoP map and the azimuth map from GT surface normal does not always align with the expected differences of π or $\pi/2$, depending on surface reflectance and sensor noise. This inconsistency leads to noisy polarization cues, which can result in inaccurate surface reconstructions

Table 2. Benchmark results on EvalMVX measured by CD in millimeter over 25 objects, where the smallest and second smallest CD values are shown in bold and underlined, respectively.

Method	MVS				MVPS				MVSfP		
	NeuS2 [40]	NeRO [28]	PET-NeuS [41]	GaussianSurfels [9]	RnbNeuS [3]	SuperNormal [4]	VMINer [11]	WildLight [8]	MVAS [6]	NeRSP [14]	PISR [7]
FACE	0.234	0.411	0.303	0.540	0.614	0.277	0.400	<u>0.250</u>	0.389	0.330	0.308
PIG	0.312	0.282	0.408	0.720	0.379	0.256	0.470	<u>0.265</u>	0.446	0.447	0.286
OWL1	0.327	<u>0.306</u>	0.360	0.636	0.443	0.288	0.319	0.342	0.354	0.371	0.423
MONKEY	0.487	0.345	0.664	0.646	0.393	<u>0.325</u>	0.530	0.335	0.365	0.501	0.311
OWL2	0.383	<u>0.321</u>	0.393	0.639	0.504	0.300	0.415	0.377	0.444	0.405	0.390
BELL	0.321	<u>0.254</u>	1.255	0.635	0.575	0.476	0.399	0.200	0.411	0.373	0.292
DUCK	0.413	<u>0.249</u>	0.717	0.684	0.739	0.637	0.548	0.268	0.490	0.685	0.245
MONK1	0.527	<u>0.401</u>	0.523	1.074	0.494	0.399	0.626	0.502	0.772	0.802	0.406
TIGER	0.385	0.382	0.520	0.703	<u>0.347</u>	0.305	0.498	0.359	0.529	0.454	0.429
SILVERDOG	0.336	<u>0.310</u>	0.432	0.618	0.355	0.280	0.555	0.324	0.520	0.363	0.313
SNAIL	0.309	0.264	0.346	0.515	0.355	0.314	0.409	<u>0.267</u>	0.486	0.320	0.344
SWAN	1.113	1.156	1.071	2.176	<u>0.971</u>	0.886	1.195	1.212	1.406	1.089	1.177
YOGA	0.452	0.284	0.738	0.675	0.549	0.510	0.426	<u>0.295</u>	0.489	0.517	0.410
HUGO	0.513	0.490	0.522	0.657	<u>0.451</u>	0.387	0.543	0.543	0.646	0.572	0.598
CHESS	<u>0.248</u>	0.262	0.266	0.507	0.286	0.240	0.373	0.282	0.497	0.353	0.324
BLACKDOG	0.337	0.393	0.428	0.597	0.322	0.262	0.387	<u>0.320</u>	0.520	0.348	0.364
MONK2	0.391	0.386	0.332	0.590	<u>0.324</u>	0.211	0.448	0.377	0.473	0.373	0.383
BIRD	0.447	0.396	0.727	0.552	<u>0.319</u>	0.330	0.781	0.263	0.591	0.481	0.474
CAW	0.421	<u>0.367</u>	0.338	0.618	0.375	0.383	0.818	0.369	0.799	0.652	0.387
KNIGHT	0.394	0.405	0.795	0.503	<u>0.363</u>	0.326	0.534	0.408	0.566	0.469	0.462
FROG	0.270	0.339	0.289	0.385	<u>0.238</u>	0.171	0.395	0.308	0.483	0.351	0.352
SPHINX	0.525	0.546	0.517	0.699	<u>0.355</u>	0.328	0.901	0.605	0.756	0.717	0.605
CAMBODIA	0.460	0.522	0.406	0.545	<u>0.291</u>	0.287	0.726	0.578	0.822	0.637	0.512
MUMMY	0.286	0.304	0.332	0.416	<u>0.172</u>	0.162	0.269	0.265	0.436	0.296	0.283
DRAGON	0.458	0.468	0.666	0.446	0.341	<u>0.387</u>	0.593	0.479	0.578	0.511	0.449
Average	0.414	0.394	0.534	0.671	0.422	0.349	0.542	<u>0.392</u>	0.572	0.497	0.421
Median	0.391	0.367	0.432	0.618	0.363	0.314	0.498	<u>0.335</u>	0.497	0.454	0.387

when adopted by MVSfP methods.

Method selection based on EvalMVX. As shown in Fig. 5, we summarize the best-performing methods and their corresponding lowest CD values for each object in EvalMVX under varying numbers of views, highlighting the working ranges and performance boundaries of current MVX methods. SuperNormal [4] demonstrates a broad applicability, effectively handling a wide spectrum of surface materials—from simple diffuse to highly reflective, owing to the strengths of photometric stereo. With per-view surface normal input, SuperNormal [4] maintains top-tier accuracy even under reduced views, showing robustness to sparse observations. Moreover, since surface normals capture fine-grained geometry, MVPS methods tend to achieve the lowest CD on objects with complex shapes, as shown in the last column. In contrast, MVSfP methods are more effective on objects with complex reflectance but relatively simple geometry, such as DUCK. MVS methods should be selected depending on surface reflectance. However, despite MVX methods get good accuracy on most object, they are still challenging for handling cast shadow (*e.g.* SWAN).

Comparison on efficiency and accuracy. As shown in Fig. 6, GaussianSurfels [9] is the fastest method among the baselines but lacks accuracy. NeuS2 [40] delivers higher reconstruction quality than GaussianSurfels [9], albeit with a slower runtime. SuperNormal [4] is the second fastest and maintains high-quality shape reconstruction, thanks to its patch-based ray marching strategy. Leveraging hash encod-

ing, VMINer [11] and PISR [7] achieve faster speeds than WildLight [8] and NeRSP [14], which rely on positional encoding. Overall, SuperNormal [4] provides a relatively optimal trade-off between computational efficiency and shape recovery quality. Note that the time for estimating normal maps is not included in this comparison.

4.3. Enhancing SuperNormal with Integrated depth

As shown in Fig. 3, SuperNormal [4] produces poor results when the input normal maps are inaccurate. To solve this problem, we incorporate per-view integrated depth as a geometric continuity regularization to improve reconstruction quality. Specifically, we apply a normal integration method [5] to get integrated depth map $\hat{\mathbf{d}}_i$ from surface normal map of the i -th view. Given depth map \mathbf{d}_i rendered by SDF, we calculate the inherent scale ambiguity s_i based on least squares, *i.e.*, $s_i = (\mathbf{d}_i^T \mathbf{d}_i) / (\hat{\mathbf{d}}_i^T \hat{\mathbf{d}}_i)$. Given this scale, we regularize the SDF network in SuperNormal [4] with an additional loss:

$$\mathcal{L}_{depth} = \sum_{i=1}^N \left| \hat{\mathbf{d}}_i s_i - \mathbf{d}_i \right|. \quad (4)$$

As shown in Fig. 7, incorporating depth regularization improves the mesh reconstruction quality of SuperNormal [4] (average CD decreases from 0.349 to 0.324). The integrated depth maps are continuous, preventing inaccurate discontinuity in recovered mesh.

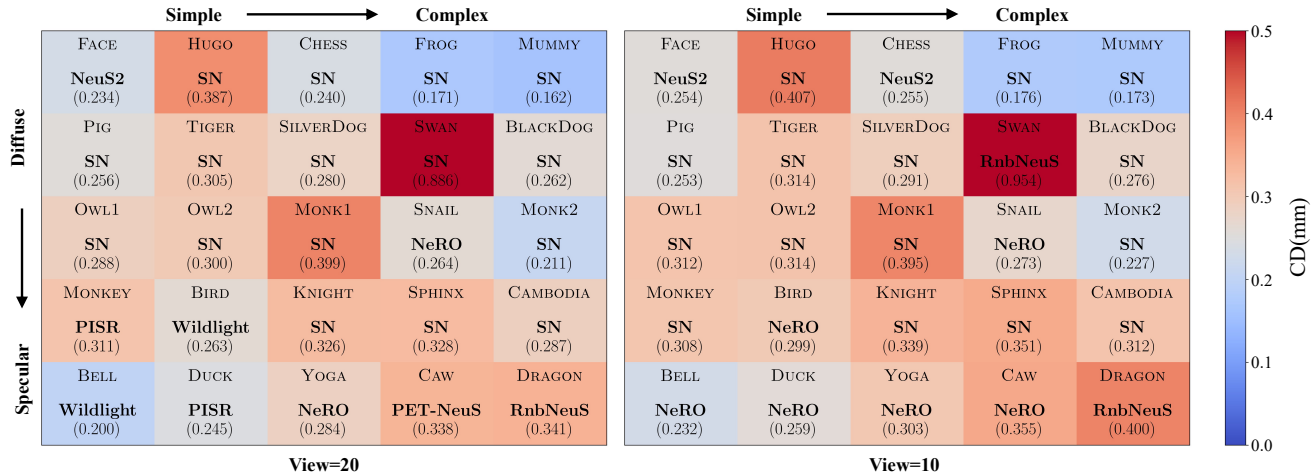


Figure 5. Best-performing method for each object in EvalMVX, with CD displayed in brackets. Summary results shown in left and right correspond to using 20 and 10 input views.

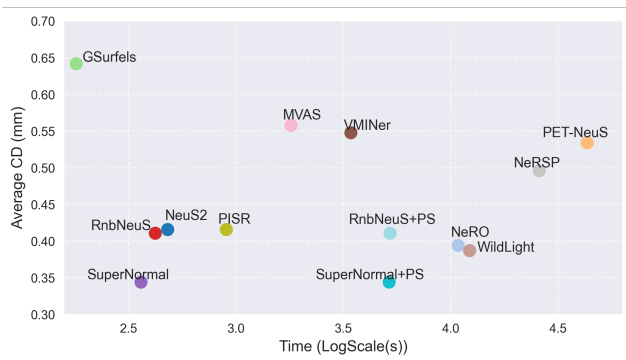


Figure 6. Visualization of accuracy and efficiency across different methods.

	Face	Pig	Owl1	Monkey	Owl2
SN	0.278	0.255	0.288	0.326	0.300
SN+Depth	0.213	0.245	0.286	0.303	0.294

	Snail	Swan	Hugo	Chess
SN	0.313	0.886	0.510	0.387
SN+Depth	0.252	0.954	0.426	0.219

	Bell	Duck	Monk1	Tiger	SilverDog
SN	0.476	0.637	0.399	0.305	0.280
SN+Depth	0.247	0.412	0.392	0.312	0.288

	BlackDog	Monk2	Bird	Caw	Knight
SN	0.261	0.211	0.329	0.383	0.326
SN+Depth	0.276	0.223	0.340	0.368	0.334

	Frog	Sphinx	Cambodia	Mummy	Dragon
SN	0.172	0.328	0.287	0.162	0.388
SN+Depth	0.181	0.330	0.302	0.174	0.328



Figure 7. SuperNormal [4] with integrated depth improves reconstructions considering per-view shape continuity.

5. Conclusion

We introduce EvalMVX, a real-world dataset designed to simultaneously evaluate MVS, MVPS, and MVSfP methods for surface shape recovery. Our benchmark results re-

veal the working range and performance of different setups across diverse shapes and reflectances. Notably, MVPS methods achieve the highest shape recovery accuracy due to the additional information provided by illumination variations, which can be conveniently obtained through flash/no-flash data capture. For accurate MVS-based shape reconstruction, NeuS2 [40] or NeRO [28] should be selected based on the reflectivity of the surface. MVSfP methods, however, show lower reconstruction quality than MVS and MVPS, primarily due to the limitations in polarization image quality from snapshot polarization cameras. Based on these findings, we identify several open problems for advancing MVX methods.

Open Problems. **1. Limitations of 3DGS Representation.** While 3DGS-based MVS offers high efficiency, its representation remains suboptimal compared to SDF due to geometric inconsistencies between 3D Gaussians and surface normals. **2. Reliability of Geometric Priors.** Surface normals estimated from learning-based photometric stereo (MVPS) and polarization cues (MVSfP) provide valuable geometric priors but are susceptible to significant errors stemming from domain gaps or sensor noise. Incorporating multiview consistency and leveraging the degree of polarization as a confidence measure could improve the robustness. **3. Efficiency of Normal Acquisition.** Although MVPS methods have shown strong performance, the surface normals produced by off-the-shelf universal photometric stereo approaches [15, 17] are computationally expensive in terms of time and memory. Developing lightweight and accurate surface normal acquisition methods is essential for enhancing the scalability and applicability of MVPS.

Limitation and future works. Our dataset evaluates 13 MVX methods across 25 objects. Given the rapid development in neural surface reconstruction, it is impractical to include every newly proposed method. To address this, we plan to develop an online evaluation platform to provide continuously updated benchmark results. Furthermore, as MVX encompasses more than just MVS, MVPS, and MVSfP, we aim to incorporate data from depth and infrared (IR) cameras and extend our dataset scale in future versions to enable broader multiview shape reconstruction evaluations beyond RGB inputs.

EvalMVX: A Unified Benchmarking for Neural 3D Reconstruction under Diverse Multiview Setups

Supplementary Material

In this supplementary material, we first provide detailed information on the capture setup and the calibration procedure for the LED light source positions. We also include the viewpoint distribution of each object to offer a better understanding of the multi-view capture settings. We then describe the complete pipeline for ground truth (GT) shape alignment, including optimization runtime and resulting alignment errors. We then show the complexity of selected objects in EvalMVX. Next, we specify the implementation details of the evaluated algorithms and include additional experiments conducted with 10 input views. We further evaluate the reconstructed meshes using mean angular error (MAE) as a complementary metric. We also report additional baseline results for further comparison. Finally, we provide the complete benchmark results containing recovered meshes and error maps reconstructed by each method on EvalMVX.

6. Capture settings

6.1. Obtaining Unpolarized RGB Images

To capture EvalMVX, we utilized a Lucid Triton RGB polarization camera equipped with a 16mm lens, obtaining raw images in Bayer format with a resolution of 2448×2048 and an exposure time of 40ms. First, the raw images were demosaiced into four single-channel polarization images: I_0 , I_{45} , I_{90} , and I_{135} , corresponding to polarization angles of 0° , 45° , 90° , and 135° , respectively. Each image has a resolution of 1224×1024 . Subsequently, we averaged the four polarization images (after replicating them across RGB channels) to obtain the depolarized RGB image, also at a resolution of 1224×1024 . Finally, a gamma correction with a gamma value of 2.2 was applied to the depolarized image to adjust their brightness and contrast, generating the final RGB images.

6.2. Viewpoints Distribution

The object is placed at the center of a circular platform and remains static during data capture. The camera is placed above the object at a slanted position and moves horizontally around the platform to capture images from multiple viewpoints. The distance between the camera and the object is maintained at a constant value of 0.6–0.8 m throughout the rotation. Fig. 8 illustrates the detailed distribution of camera viewpoints across the 25 objects.

6.3. Light Calibration

As shown in Fig. 8, the relative positions between the 16 LED lights and the camera remain fixed during image capture. The camera’s rotation matrix and translation vector in the world coordinate system are obtained through camera calibration. Based on these, the LED positions in the world coordinate system can be computed from the known camera poses and the fixed relative positions between the camera and the LEDs. Specifically, according to the CAD design of our LED rig, the LED coordinates (x, y, z) are defined in the camera coordinate system, where the optical center of the camera is assumed to be the origin. Using the calibrated camera pose, a projection matrix $\mathbf{P} = [\mathbf{R} \ \mathbf{t}]$, composed of the rotation matrix \mathbf{R} and the translation vector \mathbf{t} , is used to transform each LED’s coordinates to the world coordinate system. The coordinates of each LED in the world coordinate system (X, Y, Z) can be obtained via:

$$\begin{bmatrix} X \\ Y \\ Z \end{bmatrix} = \mathbf{R} \cdot \begin{bmatrix} x \\ y \\ z \end{bmatrix} + \mathbf{t} \quad (5)$$

7. GT Shape Alignment

As shown in Fig. 9, we scan all objects by EinScan-SP scanner. To minimize scanning errors caused by occlusions or concavities that are difficult to capture from a single viewpoint, each object was scanned in both vertical and horizontal orientations, with multiple rotations to cover all parts.

Our camera pose optimization, based on Pytorch3D [32], minimizes the discrepancy between rendered silhouette masks and the corresponding captured masks. To speed up the process, we reduce the number of faces in the GT mesh and downsample input images to a resolution of 153×128 . As shown in Table 3, this resolution reduction leads to only marginal drops in alignment accuracy (measured by the average IoU over 20 views) while significantly reducing optimization time. Thus, downsampling proves both effective and efficient. Additionally, we carefully inspected and manually corrected errors in the SAM-generated masks, as their quality greatly impacts the final results.

The optimization time depends on the object’s complexity, with all experiments performed on a single NVIDIA RTX 4090 GPU. For simple objects like FACE and DUCK, optimization for each view takes around 10 seconds, while for complex objects like CAMBODIA and DRAGON, it increases to approximately 30 seconds. We use the binary

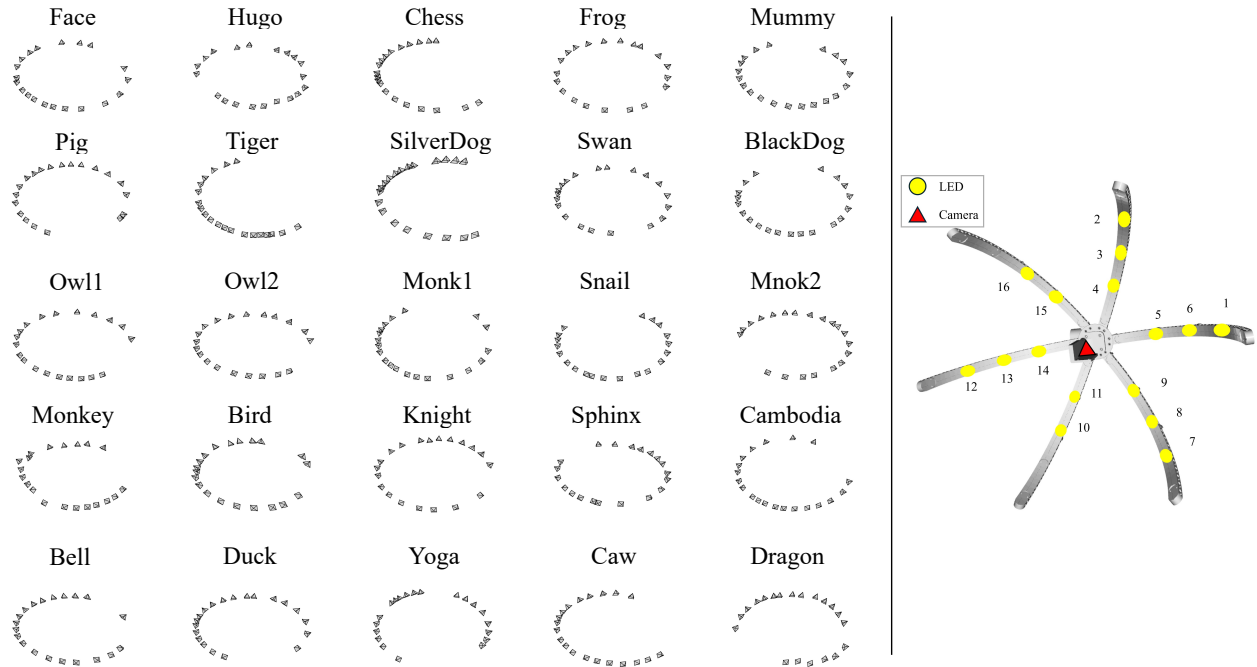


Figure 8. **(Left)** Distribution of camera poses. **(Right)** Relative positions between the LEDs and camera.

Object	Resolution	Per-view Optimization Time	Average IoU
Pig	153×128 → 1224×1024	6s → 2min	0.9910 → 0.9917
Cambodia	153×128 → 1224×1024	30s → 20min	0.9882 → 0.9891

Table 3. Comparison of mesh alignment under different resolutions.

cross-entropy (BCE) loss function, with final loss values converging between 0.0004 and 0.0006. As shown in Fig. 9, the rendered silhouettes align well with the corresponding GT masks, demonstrating the effectiveness of our multi-view silhouette-based alignment approach. After the alignment, we use Blender to inspect the results and render surface normals.

8. Shape complexity

As shown in Fig. 9, we quantify the shape complexity across different objects in EvalMVX, using average curvature [16] calculated on surface normal maps as the metric.

9. More details of benchmark evaluations

9.1. Experiment setup

We use a single NVIDIA GTX 4090 GPU for each method to run the benchmark evaluations. Notably, for RnbNeuS [3], we adopt the faster implementation RnbNeuS2, which is the official CUDA implementation of

RnbNeuS [3]. For fair comparison with SuperNormal [4], we use only normal maps as input. For GaussianSurfels [9], we experimentally found that using only RGB images as input yields better reconstruction results compared to using both the predicted normal maps from Uni-MS-PS [15] and the RGB images. Therefore, we report the reconstruction results obtained using RGB images only. Moreover, we observed that PET-NeuS [41] failed to produce valid reconstructions under the standard input setting. To ensure the method could yield usable results and allow for meaningful comparison, we manually increased the illumination intensity in the ambient input images. This adjustment was applied only to PET-NeuS [41] and not to other methods. Except for that, all other methods are evaluated using their official implementations.

Since different algorithms converge at different rates, we set varying numbers of training iterations for each method accordingly. Specifically, NeuS2 [40], SuperNormal [4], and RnbNeuS [3] are trained for 30,000 iterations; NeRO [28], PET-NeuS [41] and WildLight [8] are trained for 100,000 iterations; GaussianSurfels [9] is trained

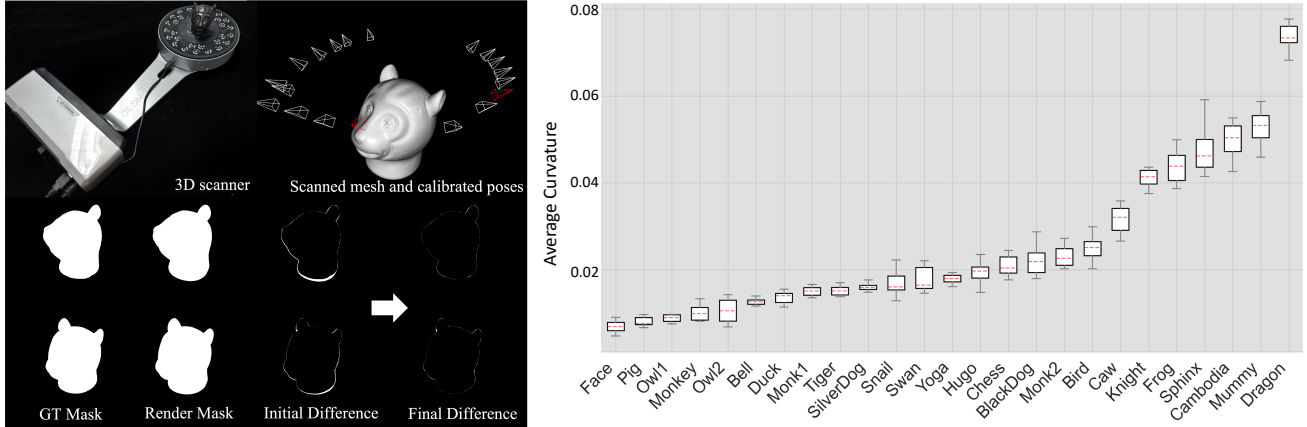


Figure 9. **(Left)** We align scanned mesh to camera views guided by GT masks. **(Right)** Curvature distribution of EvalMVX calculated from GT normals quantifies the shape complexity of each object.

for 15,000 iterations; VMIner [11] is trained for a total of 40,000 iterations; MVAS [6] is trained for 50 epochs; NeRSP [14] is trained for 50,000 iterations; and PISR [7] is trained for 20,000 iterations.

9.2. Sparse view evaluation

To evaluate the impact of reduced viewpoint numbers on the reconstruction performance of different MVX methods, we selected 10 uniformly spaced viewpoints from the original set of 20. We then evaluated the reconstruction quality of each method under this 10-view setting. The results are shown in Table 4. We observed that SuperNormal [4] and RnbNeuS [3], which rely on normal maps for surface reconstruction, remained robust even when using only half of the input views. This is likely because normal maps offer dense geometric details and enforce consistency across the surface, helping maintain smooth and accurate shapes with limited observations.

9.3. Surface normal evaluation

To further assess surface detail recovery, we compute the MAE between the ground truth and recovered surface normals across all 20 views, and report the average MAE for each object. As shown in Table 5, these results are consistent with those evaluated based on Chamfer Distance (CD). However, we observed that the evaluation may not be entirely fair to SuperNormal [4] and RnbNeuS [3], as they benefit from the accurate normals provided by Uni-MSPS [15], and continuously optimize the surface normals under multi-view constraints. Consequently, they achieve the lowest or second-lowest MAE for most objects.

9.4. Additional Baseline Results

We further evaluate the performance of the classical MVS method NeuS [39] and NeDUF [29] on EvalMVX using all

20 views, as shown in Table 6. The reconstructed meshes exhibit competitive quality across diverse objects and materials, highlighting NeuS [39] as a solid baseline for neural surface reconstruction methods.

9.5. Complete benchmark results

From Fig. 10 to Fig. 34, we present a comprehensive benchmark evaluation of the 11 methods reported in the main paper using EvalMVX. Each method reconstructs 25 objects from 20 input views, and we provide the resulting 3D shapes along with their corresponding error maps. For better visualization, the maximum distance in the error maps is truncated at 1,mm.

References

- [1] Paul J Besl and Neil D McKay. Method for registration of 3-d shapes. In *Sensor fusion IV: control paradigms and data structures*, pages 586–606. Spie, 1992. 5
- [2] Blender Online Community. *Blender - a 3D modelling and rendering package*. Blender Foundation, Amsterdam, The Netherlands, 2025. 5
- [3] Baptiste Brument, Robin Bruneau, Yvain Quéau, Jean Mélou, François Bernard Lauze, Jean-Denis Durou, and Lilian Calvet. Rnb-neus: Reflectance and normal-based multi-view 3d reconstruction. In *Proc. of IEEE Conference on Computer Vision and Pattern Recognition (CVPR)*, pages 5230–5239, 2024. 1, 2, 5, 6, 7, 3, 4
- [4] Xu Cao and Takafumi Taketomi. Supernormal: Neural surface reconstruction via multi-view normal integration. In *Proc. of IEEE Conference on Computer Vision and Pattern Recognition (CVPR)*, pages 20581–20590, 2024. 1, 2, 5, 6, 7, 8, 3, 4
- [5] Xu Cao, Boxin Shi, Fumio Okura, and Yasuyuki Matsushita. Normal integration via inverse plane fitting with minimum point-to-plane distance. In *Proceedings of the IEEE/CVF Conference on Computer Vision and Pattern Recognition*, pages 2382–2391, 2021. 7

Table 4. Benchmark results on EvalMVX with 10 views - CD evaluation in millimeter over all 25 objects, where the smallest and second smallest ones are shown in bold and underlined, respectively.

Method	MVS				MVPS				MVSfP		
	NeuS2 [40]	NeRO [28]	PET-NeuS [41]	GaussianSurfels [9]	RnbNeuS [3]	SuperNormal [4]	VMINer [11]	WildLight [8]	MVAS [6]	NeRSP [14]	PISR [7]
FACE	0.254	0.281	0.303	0.670	0.541	<u>0.260</u>	0.370	0.366	0.420	0.588	0.396
PIG	0.324	<u>0.279</u>	0.461	0.705	0.386	0.254	0.456	0.360	0.498	0.424	0.355
OWL1	0.352	<u>0.335</u>	0.423	0.759	0.424	0.312	0.541	0.532	0.419	0.424	0.439
MONKEY	0.561	0.346	0.698	0.736	0.425	0.308	0.457	0.441	0.428	0.514	<u>0.337</u>
OWL2	<u>0.391</u>	0.410	0.478	0.725	0.503	0.315	0.614	0.513	0.552	0.490	0.444
BELL	0.319	0.232	1.372	0.736	0.605	0.512	0.489	0.303	0.476	0.438	<u>0.302</u>
DUCK	0.471	0.258	0.747	0.767	0.706	0.629	0.566	0.450	0.604	0.676	<u>0.301</u>
MONK1	0.658	<u>0.423</u>	0.661	1.341	0.501	0.395	0.866	0.607	0.999	0.891	0.543
TIGER	0.400	0.383	0.494	0.772	<u>0.353</u>	0.314	0.529	0.492	0.642	0.503	0.467
SILVERDOG	0.351	0.368	0.546	0.683	0.357	0.290	0.438	0.374	0.749	0.426	<u>0.318</u>
SNAIL	0.334	0.274	0.424	0.538	0.349	<u>0.311</u>	0.415	0.403	0.569	0.375	0.360
SWAN	1.147	1.156	1.254	1.963	0.954	<u>1.053</u>	1.837	1.339	1.457	1.249	1.353
YOGA	0.474	0.303	0.999	0.741	0.522	0.563	0.706	<u>0.453</u>	0.570	0.612	0.457
HUGO	0.553	0.512	0.563	0.769	<u>0.437</u>	0.407	0.668	0.728	0.773	0.677	0.653
CHESS	0.255	0.266	0.308	0.648	0.293	<u>0.257</u>	0.384	0.334	0.550	0.478	0.361
BLACKDOG	0.356	0.359	N/A	0.700	<u>0.335</u>	0.276	0.404	0.423	0.581	0.392	0.382
MONK2	0.440	0.443	0.463	0.671	<u>0.386</u>	0.227	0.516	0.467	0.607	0.497	0.416
BIRD	0.486	0.299	1.163	0.585	<u>0.332</u>	0.386	0.705	0.595	0.604	0.452	0.510
CAW	0.541	0.355	0.500	0.634	0.411	<u>0.359</u>	0.885	0.673	1.000	0.673	0.405
KNIGHT	0.404	0.404	1.497	0.558	<u>0.344</u>	0.339	0.467	0.485	0.650	0.575	0.451
FROG	0.321	0.346	0.326	0.451	<u>0.228</u>	0.175	0.412	0.435	0.532	0.392	0.428
SPHINX	0.624	0.618	0.782	0.862	<u>0.368</u>	0.351	0.776	0.897	0.913	0.788	0.731
CAMBODIA	0.545	0.616	0.602	0.640	<u>0.315</u>	0.311	0.894	0.727	0.876	0.742	0.588
MUMMY	0.291	0.305	0.482	0.456	<u>0.176</u>	0.173	0.333	0.295	0.466	0.324	0.309
DRAGON	0.492	0.454	N/A	0.492	0.400	0.457	0.645	0.515	0.701	0.578	<u>0.441</u>
Average	0.454	<u>0.401</u>	0.676	0.744	0.426	0.369	0.615	0.528	0.665	0.567	0.470
Median	0.404	<u>0.355</u>	0.546	0.700	0.386	0.314	0.529	0.467	0.604	0.503	0.428

Table 5. Benchmark results on EvalMVX- MAE evaluation in degree over all 25 objects, where the smallest and second smallest ones are shown in bold and underlined, respectively.

Method	MVS				MVPS				MVSfP		
	NeuS2 [40]	NeRO [28]	PET-NeuS [41]	GaussianSurfels [9]	RnbNeuS [3]	SuperNormal [4]	VMINer [11]	WildLight [8]	MVAS [6]	NeRSP [14]	PISR [7]
FACE	5.96	<u>3.36</u>	4.88	12.32	4.19	2.22	6.92	3.95	8.09	7.52	14.98
PIG	9.57	<u>4.58</u>	8.84	16.53	5.62	4.15	9.40	5.06	8.86	9.60	8.69
OWL1	7.71	<u>5.17</u>	12.84	12.90	5.46	3.35	7.28	7.00	6.58	7.51	9.51
MONKEY	16.64	<u>5.62</u>	25.82	18.51	6.20	4.41	17.89	7.08	8.42	13.05	7.60
OWL2	12.35	<u>6.36</u>	11.90	17.73	7.24	3.98	10.64	9.16	9.97	10.28	11.15
BELL	12.91	<u>5.46</u>	23.41	16.95	10.55	10.32	15.12	5.36	12.83	9.41	14.56
DUCK	16.94	6.67	20.41	22.45	10.96	11.35	15.52	8.20	12.93	24.43	11.94
MONK1	13.34	9.48	14.75	22.97	<u>6.47</u>	5.59	16.55	12.96	17.06	18.60	13.35
TIGER	11.75	8.12	13.46	22.69	<u>6.03</u>	4.83	14.64	8.89	14.05	11.59	13.74
SILVERDOG	13.66	7.40	14.81	21.95	7.00	5.00	22.96	9.39	14.60	10.51	10.26
SNAIL	13.99	<u>8.24</u>	13.50	22.06	8.27	6.85	16.19	9.35	16.53	11.62	15.58
SWAN	23.18	23.75	11.69	27.13	<u>9.19</u>	8.11	23.92	23.25	25.74	16.53	24.27
YOGA	20.97	6.64	29.10	27.73	19.89	20.78	17.03	<u>8.73</u>	22.07	19.29	17.77
HUGO	15.13	12.84	13.68	19.36	<u>7.32</u>	5.93	15.04	15.46	18.76	16.16	22.27
CHESS	10.23	8.14	8.83	18.25	<u>7.24</u>	5.92	13.34	9.64	17.74	12.70	16.83
BLACKDOG	15.50	13.82	15.96	22.12	<u>10.31</u>	8.12	16.18	12.30	18.16	13.44	15.46
MONK2	14.78	12.78	11.81	22.47	<u>9.48</u>	6.67	15.72	14.63	17.49	15.00	16.33
BIRD	24.50	13.20	36.37	27.96	19.69	25.68	21.97	10.52	21.52	18.38	20.41
CAW	16.94	14.12	20.73	26.63	<u>14.79</u>	17.48	22.91	15.22	32.12	25.70	18.04
KNIGHT	20.78	17.83	25.41	27.51	12.84	<u>13.24</u>	22.26	20.80	25.29	22.10	21.73
FROG	19.31	20.32	16.67	25.50	<u>10.55</u>	8.78	22.57	20.38	26.34	22.05	26.89
SPHINX	24.87	25.35	28.67	30.00	17.59	<u>17.68</u>	33.65	25.40	31.24	29.83	30.06
CAMBODIA	26.80	27.56	25.45	30.15	15.24	<u>17.84</u>	30.87	27.30	32.44	29.64	26.87
MUMMY	22.19	21.59	18.54	27.32	<u>14.58</u>	14.16	22.93	20.95	27.82	21.60	23.96
DRAGON	33.78	32.70	35.53	37.25	29.64	32.10	35.40	33.06	40.72	34.97	34.21
Average	16.95	12.84	18.52	23.06	<u>11.05</u>	10.58	18.68	13.76	19.49	17.26	17.86
Median	15.50	<u>9.48</u>	15.96	22.47	<u>9.48</u>	8.11	16.55	10.52	17.74	16.16	16.33

[6] Xu Cao, Hiroaki Santo, Fumio Okura, and Yasuyuki Matsushita. Multi-view azimuth stereo via tangent space consistency. In *Proc. of IEEE Conference on Computer Vision and Pattern Recognition (CVPR)*, pages 825–834, 2023. 2, 5, 7, 3, 4

[7] Guangcheng Chen, Yicheng He, Li He, and Hong Zhang. PISR: Polarimetric neural implicit surface reconstruction for

textureless and specular objects. *Proc. of European Conference on Computer Vision (ECCV)*, 2024. 2, 3, 4, 5, 6, 7

[8] Ziang Cheng, Junxuan Li, and Hongdong Li. Wildlight: In-the-wild inverse rendering with a flashlight. In *Proc. of IEEE Conference on Computer Vision and Pattern Recognition (CVPR)*, pages 4305–4314, 2023. 2, 5, 6, 7, 4

[9] Pinxuan Dai, Jiamin Xu, Wenxiang Xie, Xinguo Liu,

Table 6. Extended benchmark results on EvalMVX, including the additional NeuS [39] and NeDUF [29] results.

Method	MVS					MVPS				MVSP			
	NeuS [39]	NeDUF [29]	NeuS2 [40]	NeRO [28]	PET-NeuS [41]	GaussianSurfels [9]	RnbNeuS [3]	SuperNormal [4]	VMINer [11]	WildLight [8]	MVAS [6]	NeRSP [14]	PISR [7]
FACE	0.314	0.267	0.234	0.411	0.303	0.540	0.614	0.277	0.400	<u>0.250</u>	0.389	0.330	0.308
PIG	0.292	0.343	0.312	0.282	0.408	0.720	0.379	0.256	0.470	<u>0.265</u>	0.446	0.447	0.286
OWL1	<u>0.306</u>	0.413	0.327	<u>0.306</u>	0.360	0.636	0.443	0.288	0.319	0.342	0.354	0.371	0.423
MONKEY	0.548	0.862	0.487	0.345	0.664	0.646	0.393	<u>0.325</u>	0.530	0.335	0.365	0.501	0.311
OWL2	<u>0.319</u>	0.392	0.383	0.321	0.393	0.639	0.504	0.300	0.415	0.377	0.444	0.405	0.390
BELL	0.438	0.729	0.321	<u>0.254</u>	1.255	0.635	0.575	0.476	0.399	0.200	0.411	0.373	0.292
DUCK	0.707	0.336	0.413	<u>0.249</u>	0.717	0.684	0.739	0.637	0.548	0.268	0.490	0.685	0.245
MONK1	0.348	0.519	0.527	0.401	0.523	1.074	0.494	<u>0.399</u>	0.626	0.502	0.772	0.802	0.406
TIGER	0.354	0.512	0.385	0.382	0.520	0.703	<u>0.347</u>	0.305	0.498	0.359	0.559	0.454	0.429
SILVERDOG	0.389	0.382	0.336	<u>0.310</u>	0.432	0.618	0.355	0.280	0.555	0.324	0.520	0.363	0.313
SNAIL	0.329	0.345	0.309	0.264	0.346	0.515	0.355	0.314	0.409	<u>0.267</u>	0.486	0.320	0.344
SWAN	0.804	0.743	1.113	1.156	1.071	2.176	0.971	<u>0.886</u>	1.195	1.212	1.406	1.089	1.177
YOGA	0.599	1.114	0.452	0.284	0.738	0.675	0.549	0.510	0.426	<u>0.295</u>	0.489	0.517	0.410
HUGO	0.504	0.657	0.513	0.490	0.522	0.657	<u>0.451</u>	0.387	0.543	0.543	0.646	0.572	0.598
CHESS	0.309	0.286	<u>0.248</u>	0.262	0.266	0.507	0.286	0.240	0.373	0.282	0.497	0.353	0.324
BLACKDOG	<u>0.300</u>	0.601	0.337	0.393	0.428	0.597	0.322	0.262	0.387	0.320	0.520	0.348	0.364
MONK2	<u>0.262</u>	0.266	0.391	0.386	0.332	0.590	0.324	0.211	0.448	0.377	0.473	0.373	0.383
BIRD	0.831	1.262	0.447	0.396	0.727	0.552	<u>0.319</u>	0.330	0.781	0.263	0.591	0.481	0.474
CAW	0.384	0.386	0.421	<u>0.367</u>	0.338	0.618	0.375	0.383	0.818	0.369	0.799	0.652	0.387
KNIGHT	0.464	0.648	0.394	0.405	0.795	0.503	<u>0.363</u>	0.326	0.534	0.408	0.566	0.469	0.462
FROG	0.261	0.288	0.270	0.339	0.289	0.385	<u>0.238</u>	0.171	0.395	0.308	0.483	0.351	0.352
SPHINX	0.497	0.755	0.525	0.546	0.517	0.699	<u>0.355</u>	0.328	0.901	0.605	0.756	0.717	0.605
CAMBODIA	0.377	0.554	0.460	0.522	0.406	0.545	<u>0.291</u>	0.287	0.726	0.578	0.822	0.637	0.512
MUMMY	0.438	0.299	0.286	0.304	0.332	0.416	<u>0.172</u>	0.162	0.269	0.265	0.436	0.296	0.283
DRAGON	0.637	0.567	0.458	0.468	0.666	0.446	0.341	<u>0.387</u>	0.593	0.479	0.578	0.511	0.449
Average	0.440	0.541	0.414	0.394	0.534	0.671	0.422	0.349	0.542	<u>0.392</u>	0.572	0.497	0.421
Median	0.384	0.512	0.391	0.367	0.432	0.618	0.363	0.314	0.498	<u>0.335</u>	0.497	0.454	0.387

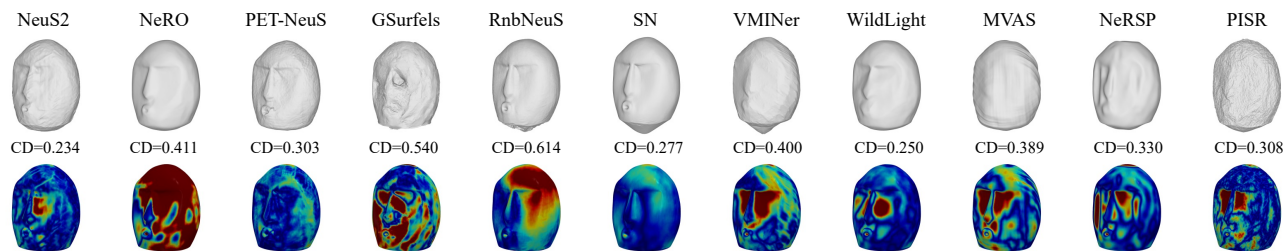


Figure 10. Recovered shapes and error maps of FACE.

Huamin Wang, and Weiwei Xu. High-quality surface reconstruction using gaussian surfels. In *Proc. of SIGGRAPH*, pages 1–11, 2024. 2, 5, 6, 7, 4

- [10] Akshat Dave, Yongyi Zhao, and Ashok Veeraraghavan. Pandora: Polarization-aided neural decomposition of radiance. In *Proc. of European Conference on Computer Vision (ECCV)*, pages 538–556. Springer, 2022. 1, 2, 3, 4
- [11] Fan Fei, Jiajun Tang, Ping Tan, and Boxin Shi. Vminer: Versatile multi-view inverse rendering with near-and far-field light sources. In *Proc. of IEEE Conference on Computer Vision and Pattern Recognition (CVPR)*, pages 11800–11809, 2024. 2, 5, 7, 3, 4
- [12] Jian Gao, Chun Gu, Youtian Lin, Hao Zhu, Xun Cao, Li Zhang, and Yao Yao. Relightable 3d gaussian: Real-time point cloud relighting with brdf decomposition and ray tracing. *arXiv preprint arXiv:2311.16043*, 2023. 2
- [13] Wenheng Ge, Tao Hu, Haoyu Zhao, Shu Liu, and Ying-Cong Chen. Ref-neus: Ambiguity-reduced neural implicit surface learning for multi-view reconstruction with reflection. In *Proc. of IEEE Conference on Computer Vision and Pattern Recognition (CVPR)*, pages 4251–4260, 2023. 2
- [14] Yufei Han, Heng Guo, Koki Fukai, Hiroaki Santo, Boxin Shi, Fumio Okura, Zhanyu Ma, and Yunpeng Jia. Nersp: Neural 3d reconstruction for reflective objects with sparse polarized

images. In *Proc. of IEEE Conference on Computer Vision and Pattern Recognition (CVPR)*, pages 11821–11830, 2024. 1, 2, 3, 4, 5, 7

- [15] Clément Hardy, Yvain Quéau, and David Tschumperlé. Uni ms-ps: A multi-scale encoder-decoder transformer for universal photometric stereo. *Computer Vision and Image Understanding*, 248:104093, 2024. 5, 6, 8, 2, 3
- [16] Moritz Heep and Eduard Zell. An adaptive screen-space meshing approach for normal integration. In *European Conference on Computer Vision*, pages 445–461. Springer, 2024. 2
- [17] Satoshi Ikehata. Scalable, detailed and mask-free universal photometric stereo. In *Proc. of IEEE Conference on Computer Vision and Pattern Recognition (CVPR)*, pages 13198–13207, 2023. 2, 3, 8
- [18] Rasmus Jensen, Anders Dahl, George Vogiatzis, Engin Tola, and Henrik Aanæs. Large scale multi-view stereopsis evaluation. In *Proc. of IEEE Conference on Computer Vision and Pattern Recognition (CVPR)*, pages 406–413, 2014. 1, 3, 4
- [19] Berk Kaya, Suryansh Kumar, Carlos Oliveira, Vittorio Ferrari, and Luc Van Gool. Uncertainty-aware deep multi-view photometric stereo. In *Proceedings of the IEEE/CVF conference on computer vision and pattern recognition*, pages 12601–12611, 2022. 1, 2

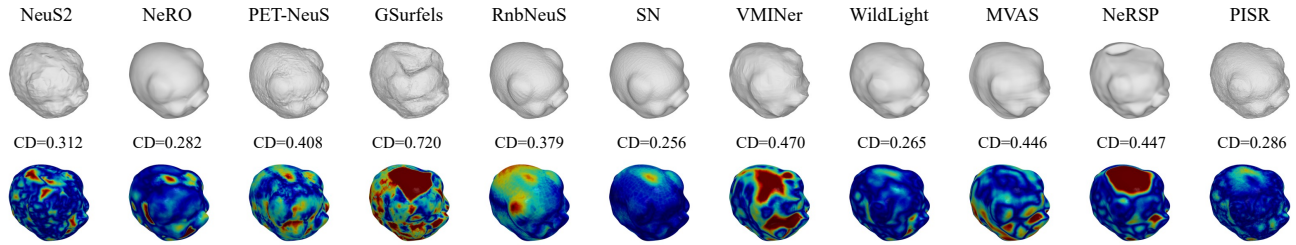


Figure 11. Recovered shapes and error maps of FIG.

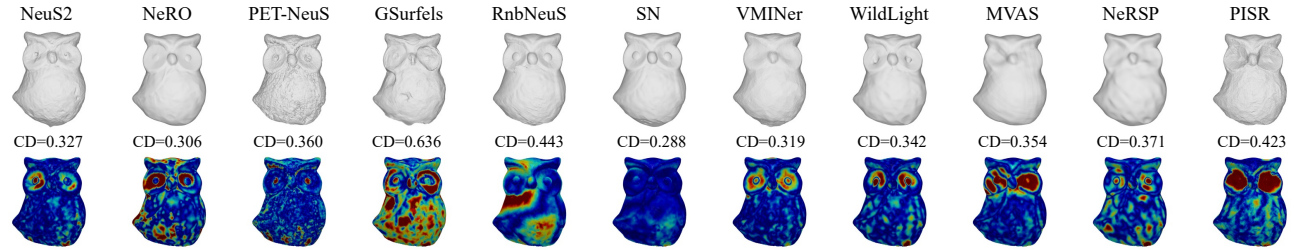


Figure 12. Recovered shapes and error maps of OWL1.

- [20] Bernhard Kerbl, Georgios Kopanas, Thomas Leimkühler, and George Drettakis. 3d gaussian splatting for real-time radiance field rendering. *ACM Trans. on Graph.*, 42(4), 2023. 2, 5
- [21] Alexander Kirillov, Eric Mintun, Nikhila Ravi, Hanzi Mao, Chloe Rolland, Laura Gustafson, Tete Xiao, Spencer Whitehead, Alexander C Berg, Wan-Yen Lo, et al. Segment anything. In *Proc. of IEEE Conference on Computer Vision and Pattern Recognition (CVPR)*, pages 4015–4026, 2023. 5
- [22] Zhengfei Kuang, Yunzhi Zhang, Hong-Xing Yu, Samir Agarwala, Elliott Wu, Jiajun Wu, et al. Stanford-orb: a real-world 3d object inverse rendering benchmark. *Proc. of Annual Conference on Neural Information Processing Systems (NeurIPS)*, 36, 2024. 3, 4
- [23] Chenhao Li, Taishi Ono, Takeshi Uemori, Hajime Mihara, Alexander Gatto, Hajime Nagahara, and Yusuke Moriuchi. Neisf: Neural incident stokes field for geometry and material estimation. In *Proc. of IEEE Conference on Computer Vision and Pattern Recognition (CVPR)*, pages 21434–21445, 2024. 1, 2
- [24] Kejie Li, Jia-Wang Bian, Robert Castle, Philip HS Torr, and Victor Adrian Prisacariu. Mobilebrick: Building lego for 3d reconstruction on mobile devices. In *Proc. of IEEE Conference on Computer Vision and Pattern Recognition (CVPR)*, pages 4892–4901, 2023. 1, 3, 4
- [25] Min Li, Zhenglong Zhou, Zhe Wu, Boxin Shi, Changyu Diao, and Ping Tan. Multi-view photometric stereo: A robust solution and benchmark dataset for spatially varying isotropic materials, 2020. 1, 3, 4
- [26] Zhaoshuo Li, Thomas Müller, Alex Evans, Russell H Taylor, Mathias Unberath, Ming-Yu Liu, and Chen-Hsuan Lin. Neuralangelo: High-fidelity neural surface reconstruction. In *Proc. of IEEE Conference on Computer Vision and Pattern Recognition (CVPR)*, pages 8456–8465, 2023. 2
- [27] Isabella Liu, Linghao Chen, Ziyang Fu, Liwen Wu, Haian Jin, Zhong Li, Chin Ming Ryan Wong, Yi Xu, Ravi Ramamoorthi, Zexiang Xu, et al. Openillumination: A multi-illumination dataset for inverse rendering evaluation on real objects. *Proc. of Annual Conference on Neural Information Processing Systems (NeurIPS)*, 36, 2024. 1, 2, 3, 4
- [28] Yuan Liu, Peng Wang, Cheng Lin, Xiaoxiao Long, Jiepeng Wang, Lingjie Liu, Taku Komura, and Wenping Wang. Nero: Neural geometry and brdf reconstruction of reflective objects from multiview images. *ACM Trans. on Graph.*, 42(4):1–22, 2023. 1, 2, 5, 6, 7, 8, 4
- [29] Yu-Tao Liu, Li Wang, Jie Yang, Weikai Chen, Xiaoxu Meng, Bo Yang, and Lin Gao. Neudf: Leaning neural unsigned distance fields with volume rendering. In *Proceedings of the IEEE/CVF conference on computer vision and pattern recognition*, pages 237–247, 2023. 5, 3
- [30] Xiaoxiao Long, Cheng Lin, Peng Wang, Taku Komura, and Wenping Wang. Sparseneus: Fast generalizable neural surface reconstruction from sparse views. In *Proc. of European Conference on Computer Vision (ECCV)*, pages 210–227. Springer, 2022. 2
- [31] Ben Mildenhall, Pratul P Srinivasan, Matthew Tancik, Jonathan T Barron, Ravi Ramamoorthi, and Ren Ng. Nerf: Representing scenes as neural radiance fields for view synthesis. *Communications of the ACM*, 65(1):99–106, 2021. 1, 2
- [32] Nikhila Ravi, Jeremy Reizenstein, David Novotny, Taylor Gordon, Wan-Yen Lo, Justin Johnson, and Georgia Gkioxari. Accelerating 3d deep learning with pytorch3d. *arXiv:2007.08501*, 2020. 5, 1

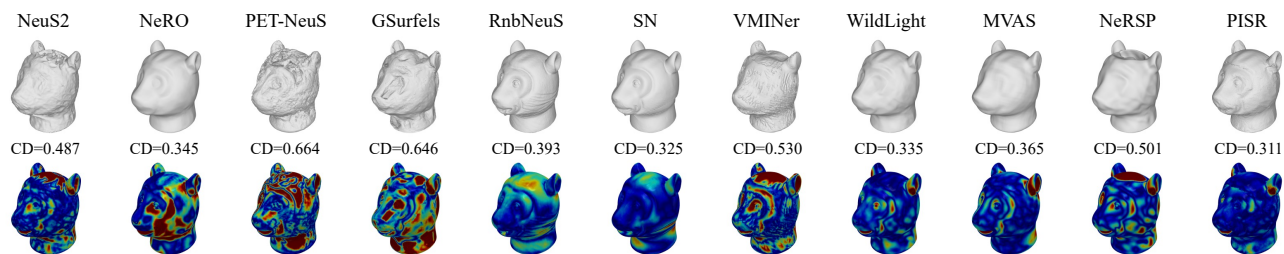


Figure 13. Recovered shapes and error maps of MONKEY.

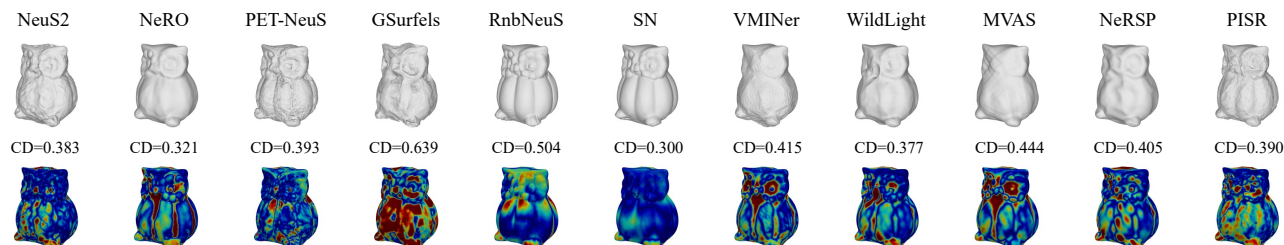


Figure 14. Recovered shapes and error maps of OWL2.

- [33] Jeremy Reizenstein, Roman Shapovalov, Philipp Henzler, Luca Sbordone, Patrick Labatut, and David Novotny. Common objects in 3d: Large-scale learning and evaluation of real-life 3d category reconstruction. In *Proc. of International Conference on Computer Vision (ICCV)*, pages 10901–10911, 2021. 3, 4
- [34] Johannes Lutz Schönberger and Jan-Michael Frahm. Structure-from-motion revisited. In *Proc. of IEEE Conference on Computer Vision and Pattern Recognition (CVPR)*, 2016. 2
- [35] Marco Toschi, Riccardo De Matteo, Riccardo Spezialetti, Daniele De Gregorio, Luigi Di Stefano, and Samuele Salti. Relight my nerf: A dataset for novel view synthesis and relighting of real world objects. In *Proc. of IEEE Conference on Computer Vision and Pattern Recognition (CVPR)*, pages 20762–20772, 2023. 1, 2, 3, 4
- [36] Benjamin Ummenhofer, Sanskar Agrawal, Rene Sepulveda, Yixing Lao, Kai Zhang, Tianhang Cheng, Stephan Richter, Shenlong Wang, and German Ros. Objects with lighting: A real-world dataset for evaluating reconstruction and rendering for object relighting. In *International Conference on 3D Vision (3DV)*, pages 137–147. IEEE, 2024. 2, 3, 4
- [37] Dor Verbin, Peter Hedman, Ben Mildenhall, Todd Zickler, Jonathan T Barron, and Pratul P Srinivasan. Ref-nerf: Structured view-dependent appearance for neural radiance fields. In *Proc. of IEEE Conference on Computer Vision and Pattern Recognition (CVPR)*, pages 5481–5490. IEEE, 2022. 2
- [38] Oleg Voynov, Gleb Bobrovskikh, Pavel Karpyshev, Saveliy Galochkin, Andrei-Timotei Ardelean, Arseniy Bozhenko, Ekaterina Karmanova, Pavel Kopanov, Yaroslav Labutin-Rymsho, Ruslan Rakhimov, et al. Multi-sensor large-scale dataset for multi-view 3d reconstruction. In *Proceedings of the IEEE/CVF Conference on Computer Vision and Pattern Recognition*, pages 21392–21403, 2023. 3, 4
- [39] Peng Wang, Lingjie Liu, Yuan Liu, Christian Theobalt, Taku Komura, and Wenping Wang. Neus: Learning neural implicit surfaces by volume rendering for multi-view reconstruction. *Proc. of Annual Conference on Neural Information Processing Systems (NeurIPS)*, 2021. 1, 2, 5, 6, 3
- [40] Yiming Wang, Qin Han, Marc Habermann, Kostas Daniilidis, Christian Theobalt, and Lingjie Liu. Neus2: Fast learning of neural implicit surfaces for multi-view reconstruction. In *Proc. of IEEE Conference on Computer Vision and Pattern Recognition (CVPR)*, pages 3295–3306, 2023. 1, 2, 5, 6, 7, 8, 4
- [41] Yiqun Wang, Ivan Skorokhodov, and Peter Wonka. Pet-neus: Positional encoding tri-planes for neural surfaces. In *Proc. of IEEE Conference on Computer Vision and Pattern Recognition (CVPR)*, pages 12598–12607, 2023. 1, 2, 5, 6, 7, 4
- [42] Haoyu Wu, Alexandros Graikos, and Dimitris Samaras. S-volsdf: Sparse multi-view stereo regularization of neural implicit surfaces. In *Proc. of International Conference on Computer Vision (ICCV)*, pages 3556–3568, 2023. 2
- [43] Tong Wu, Jiarui Zhang, Xiao Fu, Yuxin Wang, Jiawei Ren, Liang Pan, Wayne Wu, Lei Yang, Jiaqi Wang, Chen Qian, et al. Omniobject3d: Large-vocabulary 3d object dataset for realistic perception, reconstruction and generation. In *Proceedings of the IEEE/CVF Conference on Computer Vision and Pattern Recognition*, pages 803–814, 2023. 3, 4
- [44] Wenqi Yang, Guanying Chen, Chaofeng Chen, Zhenfang Chen, and Kwan-Yee K Wong. Ps-nerf: Neural inverse rendering for multi-view photometric stereo. In *Proc. of European Conference on Computer Vision (ECCV)*, pages 266–284. Springer, 2022. 2

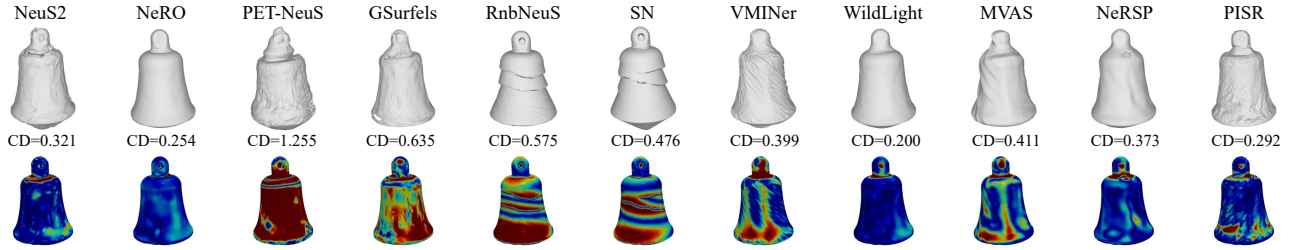


Figure 15. Recovered shapes and error maps of BELL.

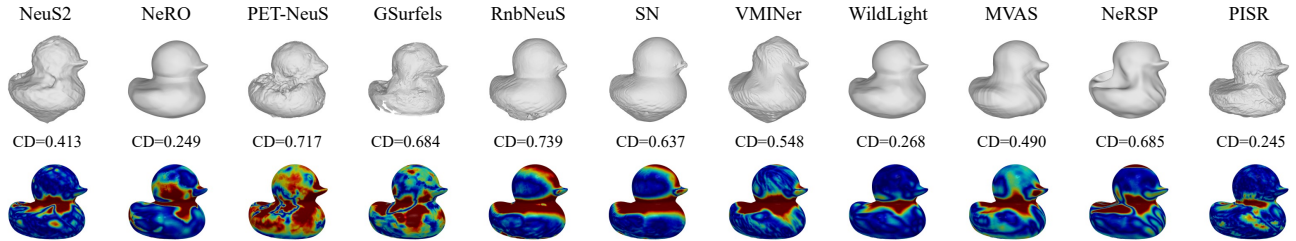


Figure 16. Recovered shapes and error maps of DUCK.

- [45] Lior Yariv, Jiatao Gu, Yoni Kasten, and Yaron Lipman. Volume rendering of neural implicit surfaces. *Proc. of Annual Conference on Neural Information Processing Systems (NeurIPS)*, 34:4805–4815, 2021. 2
- [46] Xianggang Yu, Mutian Xu, Yidan Zhang, Haolin Liu, Chongjie Ye, Yushuang Wu, Zizheng Yan, Chenming Zhu, Zhangyang Xiong, Tianyou Liang, et al. Mvimnet: A large-scale dataset of multi-view images. In *Proc. of IEEE Conference on Computer Vision and Pattern Recognition (CVPR)*, pages 9150–9161, 2023. 1, 2, 3, 4
- [47] Dongxu Zhao, Daniel Lichy, Pierre-Nicolas Perrin, Jan-Michael Frahm, and Soumyadip Sengupta. Mvpsnet: Fast generalizable multi-view photometric stereo. In *Proc. of International Conference on Computer Vision (ICCV)*, pages 12525–12536, 2023. 2

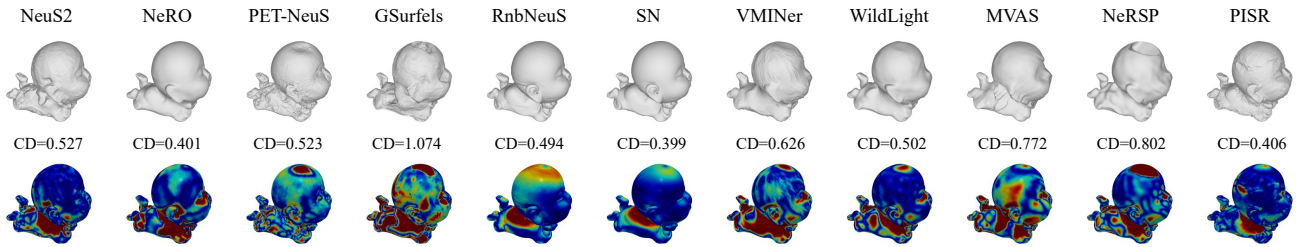


Figure 17. Recovered shapes and error maps of MONK1.

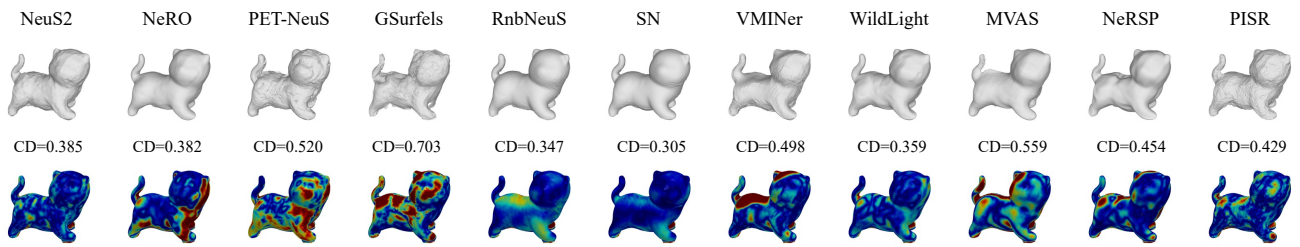


Figure 18. Recovered shapes and error maps of TIGER.

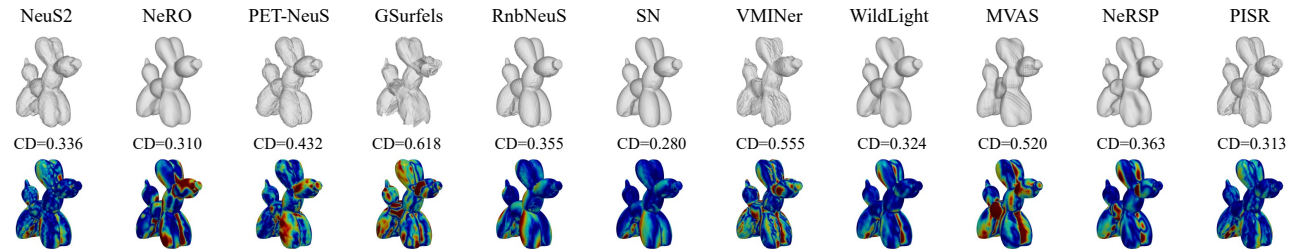


Figure 19. Recovered shapes and error maps of SILVERDOG.

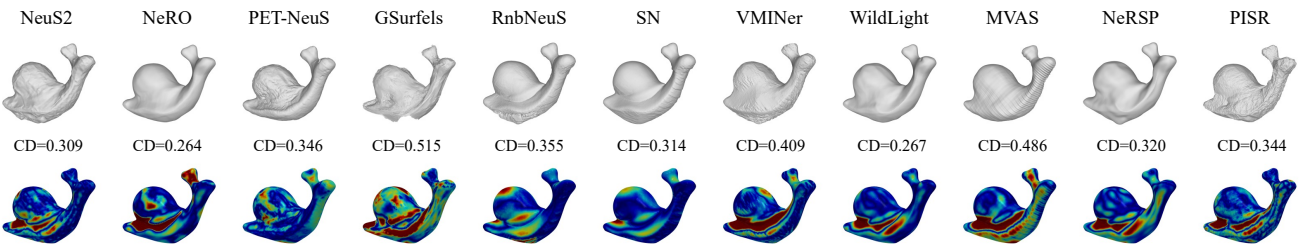


Figure 20. Recovered shapes and error maps of SNAIL.

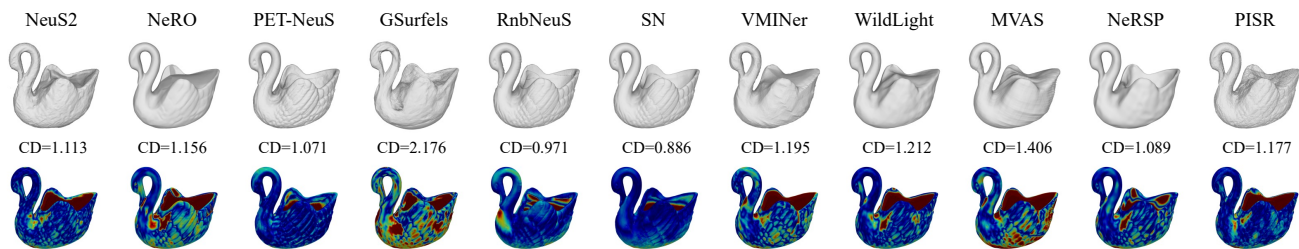


Figure 21. Recovered shapes and error maps of SWAN.

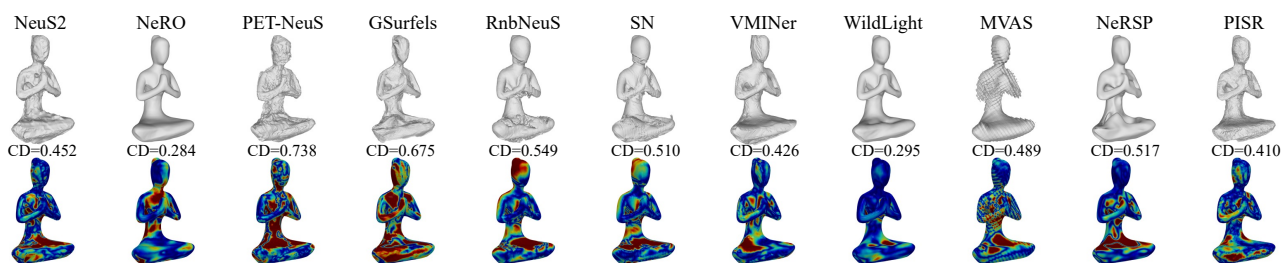


Figure 22. Recovered shapes and error maps of YOGA.

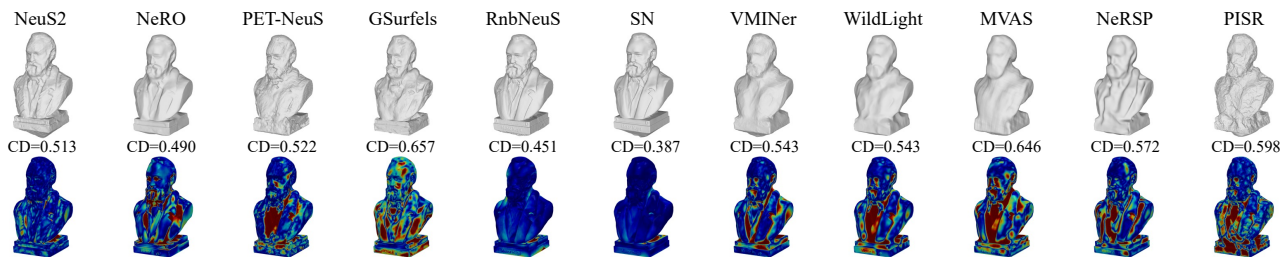


Figure 23. Recovered shapes and error maps of HUGO.

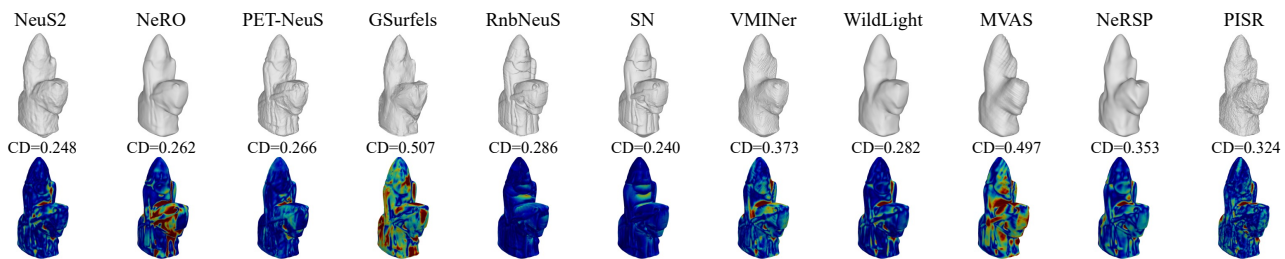


Figure 24. Recovered shapes and error maps of CHESS.

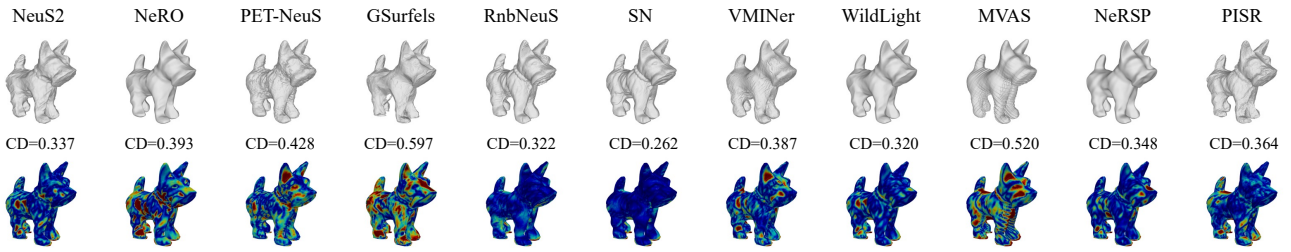


Figure 25. Recovered shapes and error maps of BLACKDOG.

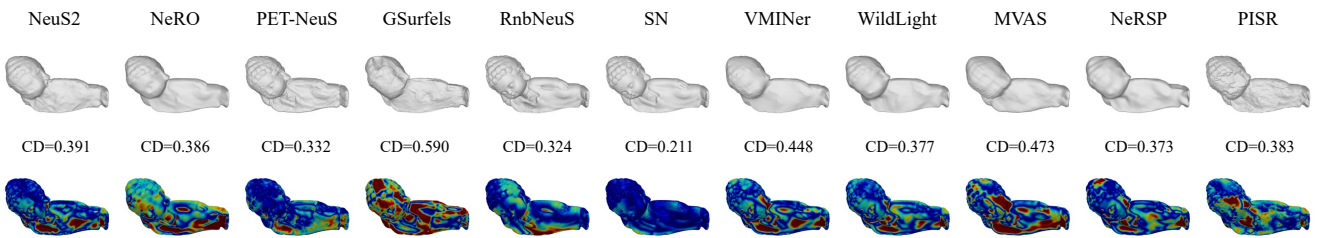


Figure 26. Recovered shapes and error maps of MONK2.

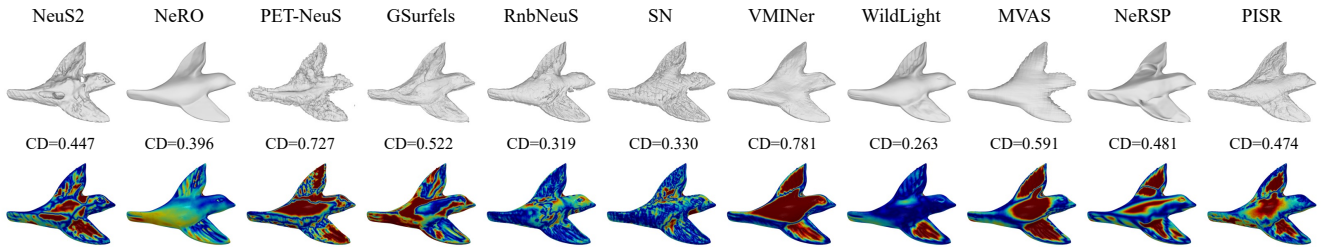


Figure 27. Recovered shapes and error maps of BIRD.

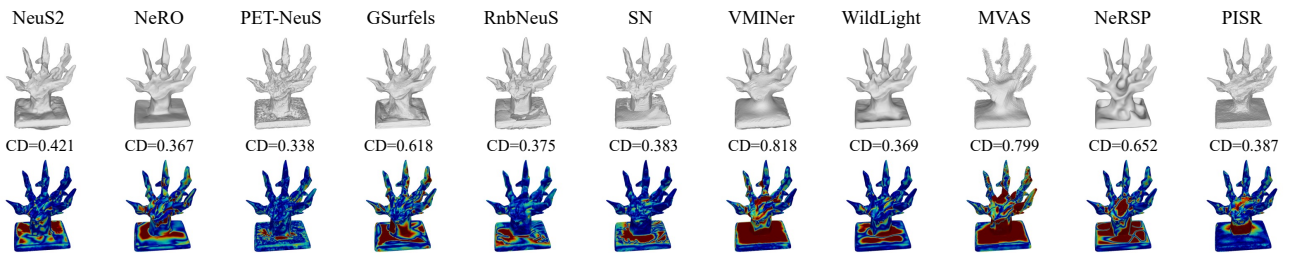


Figure 28. Recovered shapes and error maps of CAW.

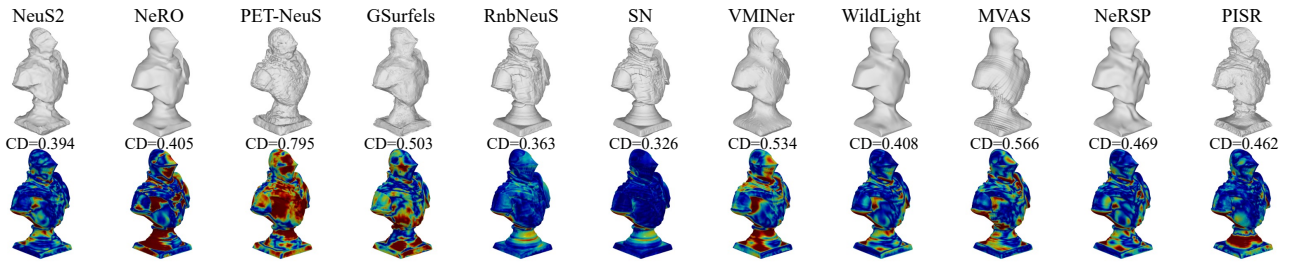


Figure 29. Recovered shapes and error maps of KNIGHT.

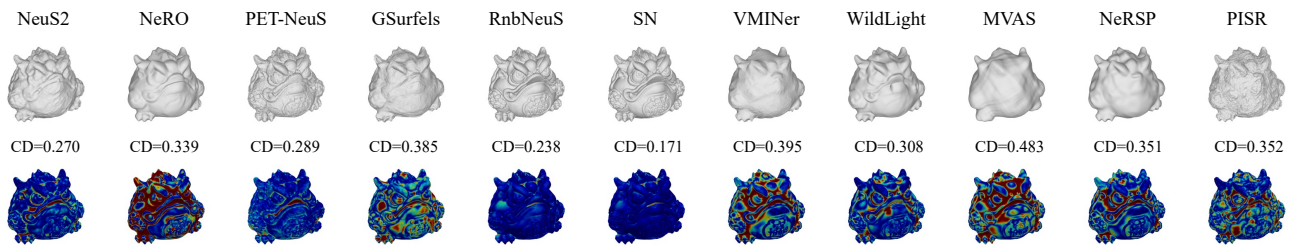


Figure 30. Recovered shapes and error maps of FROG.

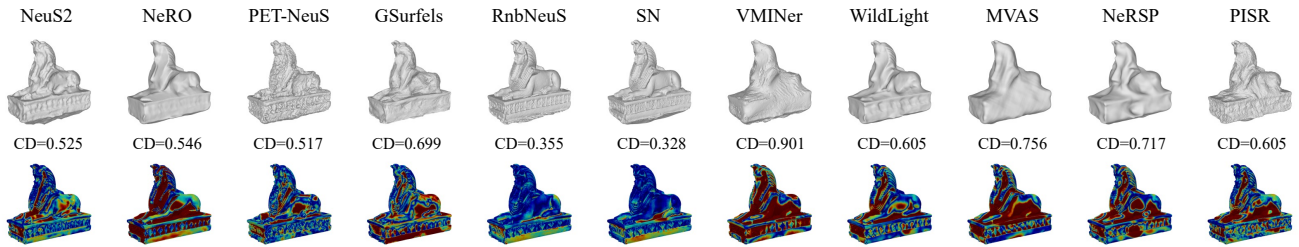


Figure 31. Recovered shapes and error maps of SPHINX.

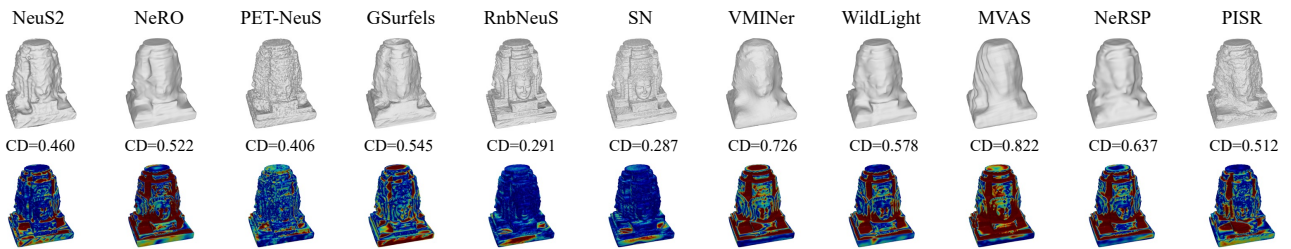


Figure 32. Recovered shapes and error maps of CAMBODIA.

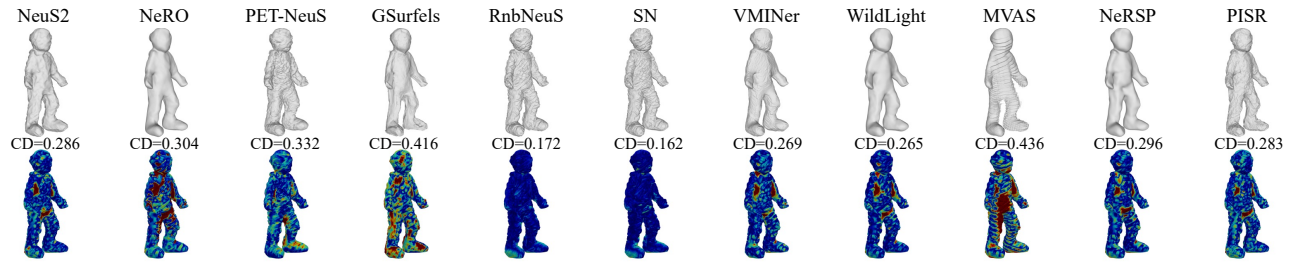


Figure 33. Recovered shapes and error maps of MUMMY.

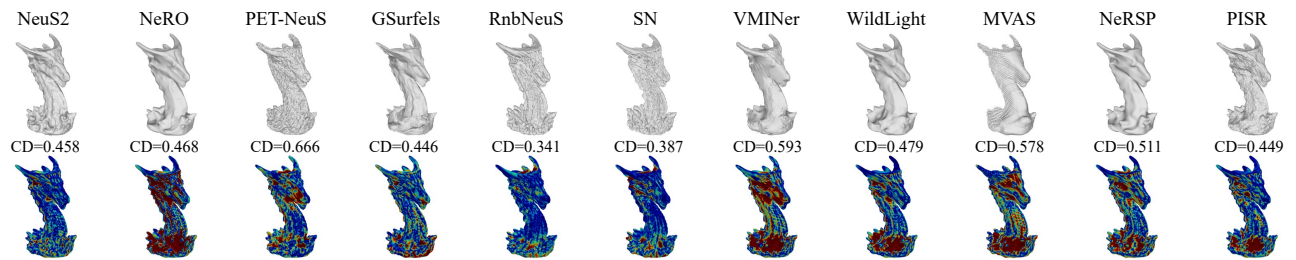


Figure 34. Recovered shapes and error maps of DRAGON.